Title

Oceanographic currents, differential subsidence, and physiography control three-dimensional clinothem growth in the Gulf of Papua, Papua New Guinea

Authors

Wei, Emily A
Driscoll, Neal W
Slingerland, Rudy L

Publication Date

2019

DOI

10.1016/j.margeo.2018.10.012

Peer reviewed

Marine Geology 407 (2019) 164–180

Contents lists available at ScienceDirect

Marine Geology

journal homepage: www.elsevier.com/locate/margo

Oceanographic currents, differential subsidence, and physiography control three-dimensional clinothem growth in the Gulf of Papua, Papua New Guinea

Emily A. Wei[a,*], Neal W. Driscoll[a], Rudy L. Slingerland[b]

[a] Scripps Institution of Oceanography, UC San Diego, 9500 Gilman Drive, La Jolla, CA, USA
[b] Department of Geosciences, Pennsylvania State University, University Park, PA, USA

ARTICLE INFO

Editor: Michele Rebesco

Keywords:
Shelf (morphology and stratigraphy)
Sequence stratigraphy
SW Pacific

ABSTRACT

A regional high-resolution CHIRP seismic survey in the Gulf of Papua (GoP) extends the geographic scope of previous studies by 125 km and reveals that the Holocene clinothem along-margin geometries, surfaces of lap, and steepness of foreset slopes appear less dependent on eustatic sea level changes and sediment supply than previously suggested. Clinothems imaged by CHIRP profiles and sampled by sediment cores include two older, relict clinothems and a younger Holocene clinothem divided into three units by two surfaces of lap. New radiocarbon ages from this study establish that depositional timing is more recent than previously proposed for the transgressive deposits, the Holocene clinothem units, and surfaces of lap. While previous ages suggested that observed stratal relationships could coincide with meltwater pulses or sea level stillstands, the younger ages from this study question these results and suggest the dominant control on Holocene clinothem architecture may be inherited physiography, SW-NE differential subsidence, along-margin currents, and seasonal variations in wave energy. Inherited physiography underlying the Holocene clinothem consists of valleys incised during relative lowstands of Marine Isotope Stages (MIS) 4 and 2. Valleys in the relict clinothem potentially served as across-margin conduits for an older Holocene clinothem unit. After the older Holocene unit filled valleys and accommodation, younger Holocene units preferentially grew along- rather than across-margin as bottom shear stresses increased. Relict clinothems have undergone differential subsidence since deposition due to foreland basin loading, which has engendered more accommodation in the northeast GoP that systematically decreases toward the southwest. Areas with less accommodation are more likely to experience toplap as they are exposed to increased shear stresses. Therefore, the surfaces of lap are caused by interactions between accommodation and oceanographic currents. Examining stratal relationships along the Holocene clinothem has broad implications for sequence stratigraphy, as many clinothems exhibit a three-dimensional stacking pattern. Measurements of seafloor slopes yield complicated results, illustrating that seafloor steepness within lobes is influenced by a complex interplay of accommodation, sediment supply, underlying physiography, and oceanographic currents. This suggests that clinothem architecture in the GoP cannot simply be interpreted as a rate-related problem between rates of sediment supply and relative sea level.

1. Introduction

In recent years, stratigraphic studies of modern and ancient clinothems have focused increasingly on the three-dimensional processes that form them. The Gulf of Papua (GoP; Fig. 1) is an ideal locale to study three-dimensional clinothem development in a high-energy setting because of its rapid sediment accumulation, active foreland basin tectonics, and seasonal oceanographic currents. Despite much research on clinothem geometry worldwide, transport mechanisms of sediment across and along clinothems are still not well understood. The GoP clinothem is a mid-shelf clinothem with three-dimensional lobate geometry suggestive of a high-energy environment (Driscoll and Karner, 1999; Slingerland et al., 2008a,b). Its downdip geometry has well-defined topsets, foresets, and bottomsets, with the highest accumulation rates occurring on the foresets (Harris et al., 1993; Walsh et al., 2004). In classic-sequence stratigraphy studies (e.g. Mitchum et al., 1977a; Christie-Blick and Driscoll, 1995), the geometries and evolution of the clinothems are viewed as a rate-related problem balancing the rate of

* Corresponding author.
E-mail address: eawei@ucsd.edu (E.A. Wei).

https://doi.org/10.1016/j.margeo.2018.10.012
Received 30 May 2018; Received in revised form 10 October 2018; Accepted 25 October 2018
Available online 27 October 2018

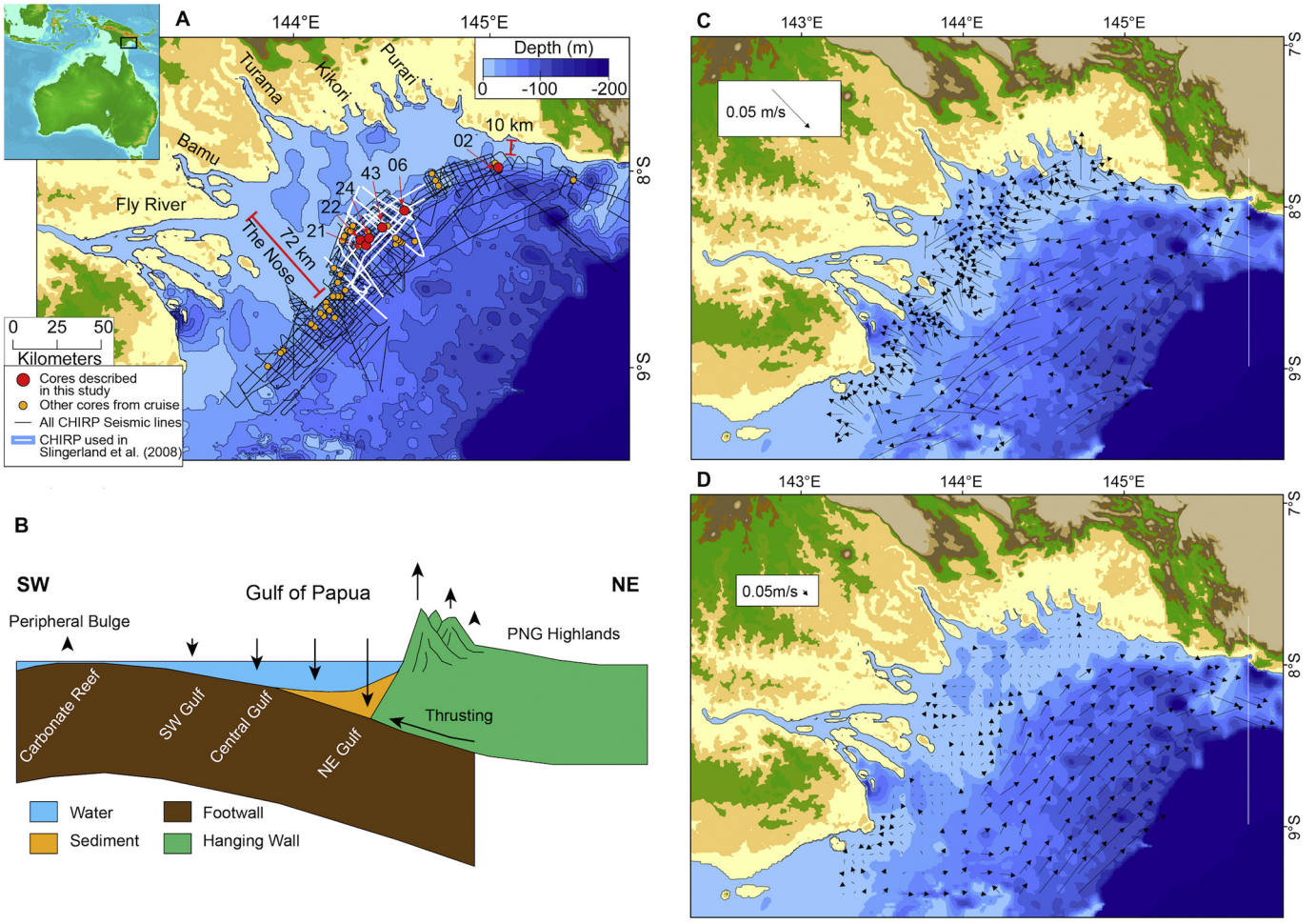

Fig. 1. A) The study area focuses on the inner shelf of the Gulf of Papua (GoP), which is highlighted by the black box in the inset. Yellow circles show the location of the 54 sediment cores. Larger red circles indicate location of cores described in this study. Black lines show the location of CHIRP seismic profiles in the entire seismic survey. A subset of these lines is highlighted in white as the seismic lines studied in Slingerland et al. (2008a). Relative shelf width decreases to the northeast, as shown by the red lines. B) Schematic cross section of the foreland basin in the Gulf of Papua. Figure modified from Christie-Blick and Driscoll (1995). C) Bottom currents during the quiescent Monsoon season. Figures C and D are modified from Slingerland et al. (2008b). D) Bottom currents during the Trade Wind season. Note different scales for Monsoon and Trade wind season bottom currents. (For interpretation of the references to color in this figure legend, the reader is referred to the web version of this article.)

sediment supply and the rate of creation of accommodation. Accommodation can be created by changes in sea level and tectonic deformation (i.e., uplift or subsidence). Though clinothem growth is often characterized by its across-margin geometry, along-margin growth controls many aspects of clinothem geometry. Numerous modeling studies (e.g., Driscoll and Karner, 1999; Ritchie et al., 2004) have shown that processes that drive modern clinothem growth include oblique and along-shelf transport from wind-driven flows, wave-orbital flows, buoyant plumes, and surf-zone processes (Nittrouer and Wright, 1994). This concept is reinforced by clinothems that grow and extend downdrift of major river systems on margins such as the Rio de Janeiro (Reis et al., 2013), the Adriatic Sea (Cattaneo et al., 2003; Cattaneo et al., 2007), the Yangtze (Xu et al., 2009), the Ganges-Brahmaputra (Kuehl et al., 1997), and the Mekong River (Nguyen et al., 2000). Along-margin transport regimes may exhibit a more regional role in the development of coastal and nearshore areas than previously considered, as along-margin currents can transport up to 30–40% of fluvially discharged sediment along the shore far from the river mouth (Liu et al., 2009). When interpreting seismic profiles that image the along-margin geometry of clinothems, challenges still exist in inverting clinothem geometry to fingerprint the process or combinations of processes that build them.

Previous sedimentological work on the GoP clinothem focused on the across-margin geometry and chronostratigraphy of relict clinothems (Harris et al., 1996; Slingerland et al., 2008a) as described in Section 2.2. This paper describes a larger area spanning ~285 km along the GoP margin, whereas the Harris et al. (1996) study area is located to the south and farther offshore and the Slingerland et al. (2008a) study area is a subset of the MARGINS survey spanning ~60 km along-margin in the Central Lobe northeast of the Fly River and offshore of the Bamu and Turama rivers (See white seismic track lines in Fig. 1). Radiocarbon ages from the Slingerland et al. (2008a) study were limited and out of chronostratigraphic order and thus more constraints on depositional timing were required. The geometry of the Holocene and relict clinothems were explained largely by eustatic sea level changes and sediment supply by Slingerland et al. (2008a). Expanded scope of the study area and new radiocarbon ages allow us to investigate other regional tectonic and oceanographic processes that contribute to the formation of the Holocene clinothem and builds on the previous results.

2. Regional setting

The GoP is a semi-circular embayment with shelf widths that progressively narrow from the southwest to the northeast, with southwest

shelf widths of 72 km and northeast widths of 10 km (Fig. 1). The southwest edge of the basin is characterized by shallow bathymetry with reef systems and Halimeda banks bordering the distal edge (i.e. peripheral bulge) of the foreland basin filled with Miocene sediment (Fig. 1; Davies et al., 1989; Pigram et al., 1989; Davies, 2012). Conversely, the northeast GoP is bordered by high mountains associated with numerous fold-and-thrust belts. Mountain building events initiated during the Mid Oligocene uplifted the Finisterre, Owen Stanley, and the New Guinea Highlands mountain ranges and formed a foreland basin to the south (Pigram and Symonds, 1991). The onset of loading heralded the transition from passive margin to a foreland basin environment as well as a transition from carbonate to detrital siliciclastic sediment deposition (Pigram et al., 1989; Tcherepanov et al., 2008). At present, the foreland basin subsides with regional rates estimated at ~1 mm/a (Slingerland et al., 2008a).

Five rivers (the Fly, Bamu, Turama, Kikori, and Purari rivers) collectively discharge approximately $15000\,m^3\,s^{-1}$ of freshwater (Wolanski et al., 1995; Fig. 1) and 365 Mt. of sediment (Milliman, 1995; Slingerland et al., 2008a) into the GoP. Discharging an average of $6500\,m^3\,s^{-1}$ of water to the GoP, the Fly River has the broadest floodplain. Despite the Fly River having the largest freshwater discharge, 40% of the Fly River sediment load is captured in its floodplain (Day et al., 2008). Although river discharge can have minor seasonal variations (Warrick et al., 2004), the largest fluctuations in discharge result from El Niño climatic conditions, which decrease rainfall, reducing water and sediment discharge (Dietrich et al., 1999; Ogston et al., 2008). When sediment discharge from the rivers is hyperpycnal, it moves as fluid muds by gravity flows that travel from the river mouth, are temporarily deposited on the clinothem topset and subsequent reworking advects it downslope to the foreset and bottomset. Conversely, hypopycnal flows carry sediment in suspension, where the sediment is advected by wind-driven and baroclinic currents and eventually deposited when energy decreases (Wolanski and Alongi, 1995; Wolanski et al., 1995; Harris et al., 1993; Walsh et al., 2004; Keen et al., 2006; Ogston et al., 2008).

2.1. Oceanographic setting

Circulation in the Gulf of Papua modulates the location of erosion and deposition as well as influences the along- and across-shelf transport of sediment. GoP circulation is complex and spatially heterogeneous due to baroclinic currents, wind-driven currents, and the region's variable morphology (Slingerland et al., 2008b).

In general, the main forces that resuspend noncohesive mud are spring-neap tidal currents and seasonal bottom currents, as the conditions that allow for sediment resuspension and the generation of gravity flows are peak spring tides during the trade wind season (Martin et al., 2008; Slingerland et al., 2008b). Tides in the GoP have a strong spring-neap variation, are directed across-shelf, and amplified on topsets (Slingerland et al., 2008b). Near-bed tidal currents can reach 0.76 m/s on the clinothem topset, whereas upper foreset currents can reach 0.64 m/s during spring tides (Slingerland et al., 2008b). As a result, spring tides can produce shear stresses capable of resuspending fine sand and noncohesive mud (Walsh et al., 2004).

The largest control on circulation is seasonal changes in energy (i.e., monsoon versus trade wind). Shifting wind patterns can create gyres that can cause subsequent shifting of currents on timescales of hours, weeks, and seasons (Slingerland et al., 2008b). During the winter Monsoon season (December to March), northwest winds on the order of 1–2 m/s generate a persistent eddy in the north GoP and a clockwise gyre over the gulf (Fig. 1C; Slingerland et al., 2008b). These conditions generate weak landward bottom currents that reach a peak of 0.04 m/s during spring tides whereas net conditions are 0.02 m/s (Slingerland et al., 2008b). The quiescent Monsoon season allows for temporary sediment storage on the shallow topset bed at depths < 10 m (Walsh et al., 2004). Conversely, the stronger and sustained southeast Trade Winds (prevalent from May through October), with velocities ~4–5 m/s, cause a convergence of flow north of the clinothem that then results in a counterclockwise gyre (Slingerland et al., 2008b). Trade wind conditions generate near-bed currents that are weaker (0.01–0.03 m/s) over the topset and increase to 0.05–0.1 m/s at the foreset; even though in general bottom currents during the trade wind season are stronger than those during the monsoon season (Fig. 1D; Slingerland et al., 2008b). Bottom currents over the foreset during the trade wind season may be responsible for the advection of illite-rich Fly River sediment to the northeast (Slingerland et al., 2008b).

In the GoP as well as many delta-scale subaqueous clinoforms (e.g., the Amazon, the Adriatic Sea, and the Atchafalaya) around the world, sediment accumulation is largely focused on the foreset with little deposition on the topset and bottomset (Kuehl et al., 1986; Walsh et al., 2004; Neill and Allison, 2005; Puig et al., 2007; Patruno and Helland-Hansen, 2018). Traditionally, clinothem topsets are expected to experience higher energy conditions than the foreset or bottomset, where the clinothem rollover indicates the limit below which wave-current shear stresses decreases (Cattaneo et al., 2007; Nittrouer et al., 1986; Kuehl et al., 1986; Walsh et al., 2004). Elevated near-bed shear stresses at the topset beds may result in bypass caused by resuspension of topset sediment that is advected to the foreset (Nittrouer and DeMaster, 1996). Such is the case in the Gulf of Papua, where sediment on topset beds are eroded and winnowed during the trade wind season (Walsh et al., 2004; Slingerland et al., 2008b). The mechanisms that resuspend and mobilize sediment are a combination of spring tidal currents, waves, and storm surges acting in concert with strong bottom currents during the trade wind season (Harris et al., 2004; Ogston et al., 2008; Slingerland et al., 2008b). Once these currents generate the necessary shear-strength to resuspend sediment, mobilized sediment in concentrations $> 10\,mg\,l^{-1}$ may form fluid muds that move down the clinothem foreset until halted by drag (Slingerland et al., 2008b). Although peak spring tide conditions during the trade wind season are the most effective at transporting bottom sediment along and across margin, these transport regimes are episodic and spatially heterogeneous (Slingerland et al., 2008b). As bottom currents are not directed seaward during either the trade wind or monsoon season (Fig. 1C and D), deposition on the clinothem foreset occurs via downslope movement of fluid mud (Slingerland et al., 2008b) and appear similar to fluid mud processes that built the Amazon subaqueous clinothem (Kineke et al., 1996). Similar temporary sediment storage and advection on the topset is observed in the Atchafalaya clinothem in the Gulf of Mexico where the passage of occasional cyclonic storms resuspends topset sediment and supplies it to the foreset (Neill and Allison, 2005).

2.2. Previous studies on the GoP inner shelf clinothem

Stratigraphy in the GoP inner shelf clinothem has been previously described by Harris et al. (1996) and Slingerland et al. (2008a). Here we summarize the findings of previous research in the GoP. Although the Slingerland et al. (2008a) study referred to sediment units as colors, we prefer to name the units alphanumerically as A1, A2, A3, B1, B2, C, and D because this practice has become more standard in recent seismic stratigraphy studies (e.g., McHugh et al., 2010; Hogarth et al., 2012). To relate nomenclature from Slingerland et al. (2008a) to this study, please refer to Table 1. Interpretations from Slingerland et al. (2008a) were confined to an area that they defined as the “central lobe.” To maintain consistency and to orient the reader, we will refer to this central area as the Central lobe and will refer to the adjacent areas as the Southern and Northern lobes.

Three distinct clinothems are observed in the Gulf of Papua (Figs. 2 and 3 from this study). Although the geometry and morphology of the margin is largely influenced by the most recent Holocene clinothem, the two underlying relict clinothems exert important controls on the architecture of the Holocene clinothem. As described by Harris et al. (1996) and Slingerland et al. (2008a), the margin consists of stacks of

Table 1
Units described by Slingerland et al. (2008a) and this study.

Name (Slingerland et al., 2008a)	Unit color in seismic profiles	Unit name (this study)	Upper bounding surface	Relative Age (Slingerland et al., 2008a)	Relative age (this study)
Red	Red	Unit A1	Seafloor	< 1.6 ka	< 112 years BP
Orange	Orange	Unit A2	Surface of lap S2		112–1570 years BP
Yellow	Yellow	Unit A3	Surface of lap S1	> 2.41 ka or > 5.2 ka	3835–1570 years BP
	Green	Unit B1			3835–6561 years BP
	Cyan	Unit B2	Undulatory boundary		9.5–10.3 ka
Relict clinothem	Blue	Unit C		Marine Isotope Stage (MIS) 3	MIS 3
Relict oblique clinothems	Pink	Unit D		MIS 4	MIS 5a – MIS 4

two relict and eroded clinothems and a smooth younger clinothem. The two older clinothems are herein referred to as separate units; however, the smooth, youngest clinothem was divided into three units by Slingerland et al. (2008a). The three clinothems are separated by two prominent regional unconformities. The older and deeper regional unconformity truncates prograding reflectors and separates the basal unit from an overlying unit with horizontal reflectors. The unit with prograding reflectors, herein referred to as Unit D, is the most basal unit observed in this survey and is separated from the overlying Unit C by a regional unconformity. Horizontal reflectors in Unit C are truncated by a younger regional unconformity that separates Unit C from Unit B, which also has horizontal reflectors that infill topographic lows (Slingerland et al., 2008a). Within the Holocene clinothem are two bounding surfaces that separate it into three units.

Unit D is shown in an uninterpreted dip profile from the southwest portion of the survey and is characterized by tangential oblique clinoforms (see Fig. 4a from Slingerland et al., 2008a; Mitchum et al., 1977b). Based on the prograding geometry, this unit is inferred to have been deposited during MIS 4 (Slingerland et al., 2008a; Fig. 3). This basal unit is mantled by Unit C and is separated by an angular unconformity (Fig. 3; Slingerland et al., 2008a). Unit C (shown in blue) is interpreted to have been deposited during MIS 3 and is characterized by aggrading reflectors and an erosional upper boundary that truncates reflectors (Figs. 2 and 3; Slingerland et al., 2008a). This erosional surface has created the so-called corrugated “Mesa topography” (Harris et al., 1996), on top of which the Holocene clinothem has been deposited. In order to have accommodation sufficient to create aggradational beds at this time, the gulf required regional subsidence rates on the order of ~1 mm a^{-1} (Slingerland et al., 2008a).

Sedimentary deposits between the Unit C and the Holocene clinothem are characterized by two facies (Harris et al., 1996). The younger facies contains abundant benthic foraminifers, molluscs, echinoid fragments, bryozoan, and Halimeda and was dated to ~6160 years BP (Harris et al., 1996). The older facies is a peat bed dated to ~16,750 years BP (Harris et al., 1996). Based on the dates and facies descriptions, these deposits were interpreted to have been deposited during the post-glacial sea level rise and we will refer to them as Unit B1. Unit B1 is not continuous but rather is localized in topographic lows incised into Units C and D. The boundary between Unit B1 and the overlying Holocene clinothem is defined by downlap of Holocene clinothem sediment onto horizontal beds in Unit B1 (Slingerland et al., 2008a).

Downlapping onto Units B1 and C is the Holocene clinothem, which is separated into three units by two surfaces of lap defined as the older S1 and younger S2 (Fig. 2; Slingerland et al., 2008a). S1 and S2 were identified as surfaces that terminate underlying units through top- or offlap (Slingerland et al., 2008a). Overlying units may exhibit on- or downlap onto the S1 or S2 surfaces. The S1 surface was interpreted by Slingerland et al. (2008a) to represent an erosional unconformity or a surface of bypass. Although these Holocene units were referred to by

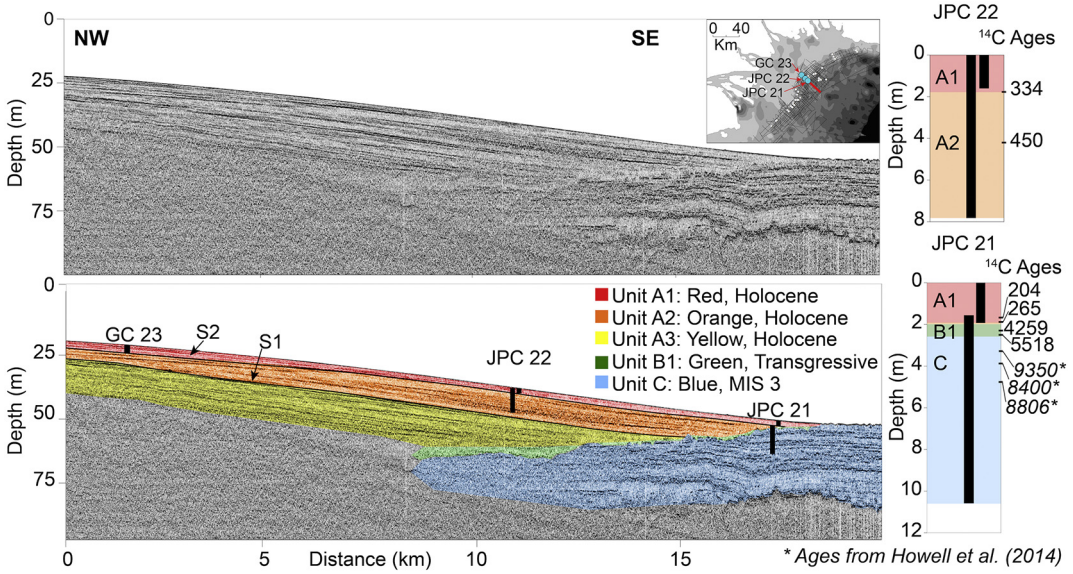

Fig. 2. CHIRP seismic dip profile images the four main sediment packages formed along the margin. The bottommost sequence in this profile, Unit C (blue), has horizontal reflectors. This is overlain by thin deposits of Unit B1 (green). Units A3, A2, and A1 (yellow, orange, and red) comprise the Holocene clinothem. Three reflectors (Yellow, Blue, and Lime green) within A2 are correlated to sediment cores. The locations of three sediment cores, GC23, JPC22, and JPC21 are shown as topset, foreset, and bottomset cores, respectively. For JPCs 21 and 22, both the trigger and piston cores are projected onto the seismic line. Inset shows location of the seismic line (highlighted in red) and cores GC23, JPC 22, and JPC 21 (highlighted in blue). At right, an expanded view of the cores shows corrected radiocarbon ages relative to depth in the core. (For interpretation of the references to color in this figure legend, the reader is referred to the web version of this article.)

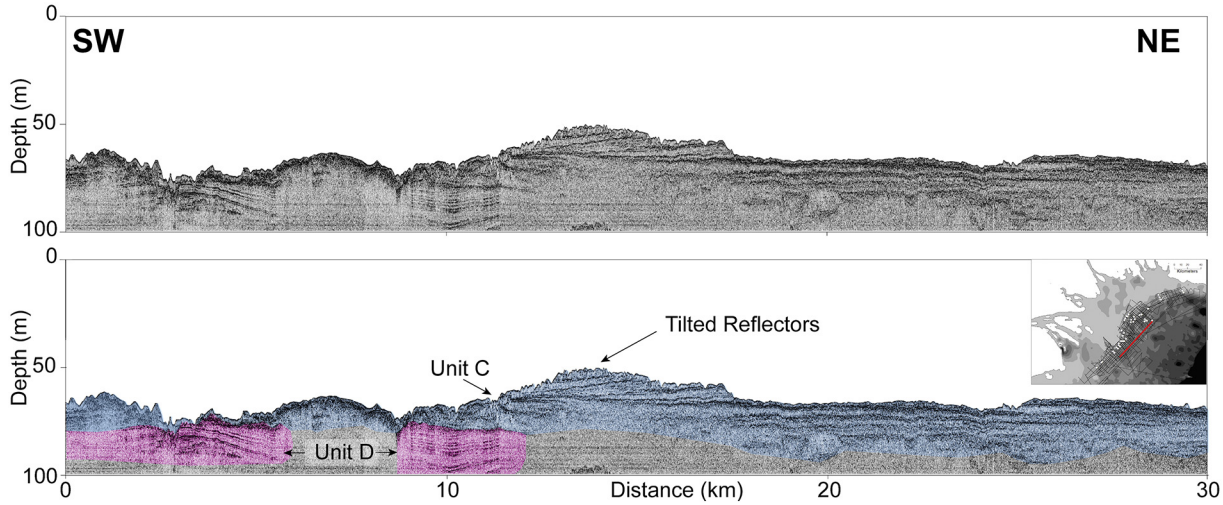

Fig. 3. A strike line of the so-called "Mesa" topography comprised of Unit C and underlying Unit D. Horizontal beds in Unit C are overlain in some locations by tilted reflectors. The upper boundary of Unit C is eroded with marked truncation. Unit D exhibits across-margin dipping geometry, and in strike profiles, the northeast dip is the consequence of three-dimensional clinothem growth. Inset shows location of the seismic line (highlighted in red). (For interpretation of the references to color in this figure legend, the reader is referred to the web version of this article.)

their color (Yellow, Orange, and Red) by Slingerland et al. (2008a), we will refer to them as Units A3, A2, and A1, respectively (Table 1). The oldest Unit A3 (Yellow in Fig. 2) is separated from the overlying Unit A2 (Orange in Fig. 2) by S1. Radiocarbon ages from bivalves above and below the S1 surface constrain the surface between 2.41 and 5.2 ka (Slingerland et al., 2008a). Given this time interval has no rapid rises in sea level, the authors speculated that S1 was caused by a decline in sediment supply (Slingerland et al., 2008a). The most recent package A1 (Red in Fig. 2) drapes the clinothem, has nearly uniform thickness, and is characterized by three aggrading high-frequency low-amplitude reflectors (Fig. 2). It is separated from the underlying package by S2, another surface of lap (Slingerland et al., 2008a). Slingerland et al. (2008a) do not provide a hypothesis for the formation of the S2 surface of lap. Isopach maps of Units A2 and A1 show that sediment is generally thicker on topographic highs and pinches out in valleys (Slingerland et al., 2008a). The thickness variability mapped through Units A3, A2, and A1 suggest that the growth of the Holocene clinothem was via along-shelf oblique transport in a northeast-southwest-trending direction, consistent with northeast-directed bottom currents during the Trade-Wind season (Slingerland et al., 2008a,b). Predominant northeast advection also explains patterns of clay mineralogy, with high illite:smectite ratios proximal to the Fly River, a mixing zone of intermediate values, and low illite:smectite ratios proximal to the northeastern rivers (Slingerland et al., 2008a).

3. Materials and methods

3.1. CHIRP seismic data

Between September 2003 and March 2004, 6800 km of Compressed High Intensity Radar Pulse (CHIRP) data were collected onboard the R/V Melville as part of the NSF MARGINS Initiative (Fig. 1). Of these lines, 2300 km were collected with the Scripps Institution of Oceanography surface-towed Edgetech profiler with a 500 Hz–6 kHz signal and a 50 ms sweep and navigation of the surface-towed CHIRP was derived from comparing the fish depth and winch cable payout relative to the ship topside DGPS receivers. In addition, 4500 km of data were acquired with a Knudsen hull-mounted profiler with a 3.5 kHz center

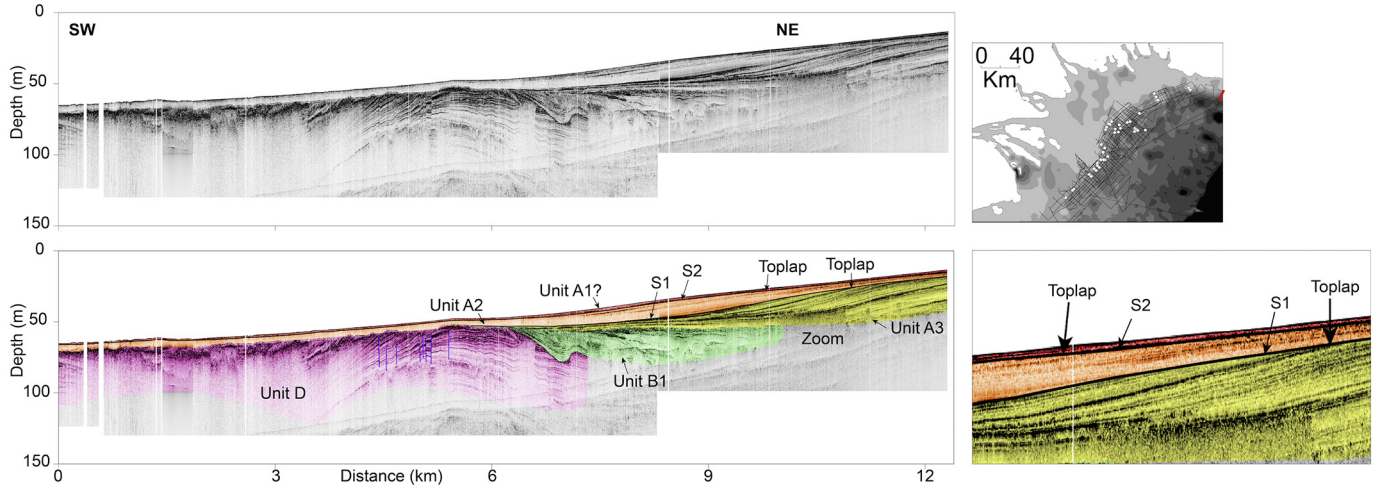

Fig. 4. Deformation is observed in Unit D and the overlying channel deposit (green). An E-W trending antiform is crosscut by numerous vertical faults. The Holocene clinothem sediment (Units A3, A2, and A1) downlaps the anticline and exhibits little to no deformation. White striping represent data gaps. Map inset shows location of the seismic line highlighted in red. Below this, a section on the clinothem foreset is enlarged to show toplapping reflectors at the S2 and S1 surfaces. (For interpretation of the references to color in this figure legend, the reader is referred to the web version of this article.)

frequency. For both systems, vertical resolution is submeter to depths of ~50 m. Cruise track spacing was designed to provide dip line coverage of clinothem geometry as well as detailed strike-line coverage of along-shelf variability (Fig. 1A). Although no new seismic data were acquired in the GoP since Slingerland et al. (2008a), that study used only a subset of Edgetech profiler seismic lines located in the Central GoP, whereas this study uses Edgetech profiler and Knudsen profiler lines across the entire GoP (Fig. 1A).

Initial processing, including ship heave removal and gain adjustment were performed using SIOSEIS (Henkart, 2003) and Seismic Unix (Cohen and Stockwell, 2001). Lines were then imported into Kingdom Software, where basic sequence stratigraphic principle, that is identifying changes in stratal geometry (e.g., Mitchum et al., 1977a,b; Vail et al., 1977; Christie-Blick and Driscoll, 1995) were employed to identify and interpret sediment packages as well as trace strong reflectors in the Holocene units. Once interpreted, Kingdom Software aided in determining depths to interpreted surfaces by converting two-way travel time to depth in meters (See Section 3.2). Depths of lower surfaces were subtracted from upper surfaces to compute thicknesses of intervening units. Data points with thickness values were converted into interpolated grid surfaces using a continuous curvature surface algorithm with an interior tension of 0.60 in Generic Mapping Tools (GMT; gmt.soest.hawaii.edu). Interpreted seismic profiles and their corresponding navigation were loaded into Fledermaus Software by Interactive Visualization Systems to create three-dimensional perspective views.

3.2. Sediment Cores

CHIRP subbottom profiles were used to select the locations of 27 jumbo piston core (JPC) and 21 gravity core (GC) locations across the shelf during the MARGINS campaign (Fig. 1A). Trigger cores (TC) were deployed with the JPCs. In some cases, drift in ship position caused the cores to be offset from the profiles, in which case the core locations were projected orthogonally onto the profile. On board, whole intact cores were scanned for magnetic susceptibility, gamma density, P-wave velocity, and resistivity using a GeoTek Core-logger. Cores were split and observations of colour, grain size, sediment structures, and general lithology were recorded. The entire suite of cores collected during the 2004 MARGINS campaign were analyzed and described in this study. Detailed description and sampling are presented for JPCs 01, 02, 06, 17, 21, 22, 24, and 43. Slingerland et al. (2008a) presented results from JPCs 40 and 43 and Howell et al. (2014) examined JPCs 01, 13, 21, and 48.

A total of 39 samples were collected for radiocarbon dating, preferentially from benthic foraminifera (*asterotalia*), as planktonic foraminifera abundance was insufficient for radiocarbon dating. The samples were analyzed at the Center for Accelerator Mass Spectrometry at Lawrence Livermore Laboratory and produced an age using the Libby half-life of 5568 years and following the convention of Stuiver and Polach (1977). The ^{14}C ages were converted using the IntCal13 program (Reimer et al., 2013) with a δ_R value of 10.

Radiocarbon dates of the top of the piston core and the bottom of the trigger core indicate that some of the piston cores overpenetrated the sediment during deployment, which was the result of sampling in shallow water (< 200 m) that limited the rebound of the trawl wire when the piston core was triggered. Though modern radiocarbon ages of the tops of the trigger core indicate that they recovered surficial sediment, ages older than one hundred years suggest that many of the piston cores did not recover surficial sediment. Offset between the trigger and piston cores were calculated in the following manner. Sedimentation rates between the bottom and top of the trigger core were calculated. This rate was multiplied by the age of the top of the JPC to find its true depth. JPC 22 and 24 were found to have no offset between the trigger and piston cores. However, JPCs 02, 06, 17, 21, and 43 had offsets ranging from 1.6 to 4.26 m (this study; Marcuson et al., 2014).

To correlate the cores to the seismic profiles, two-way travel times were converted to depth using a sound velocity of 1300 m/s in contrast to the 1750 m/s used by Slingerland et al. (2008a). We first estimated the sound velocity of the sediment by averaging P-wave velocity measurements from the GeoTek Core logger to obtain a value of ~1350 m/s. Downcore P-wave velocity reveals that muddy sediments have P-wave velocities averaging ~1500 m/s and sandy layers have average P-wave velocities ~1000 m/s. We verified the sound velocity by matching the distinct shift in core facies to seismic profile unconformities between the MIS 3 unit and the overlying transgressive and Holocene units and found a sound velocity of 1300 m/s matched the facies boundaries to the seismic profiles better than a sound velocity of 1350 m/s. Though 1300 m/s is low compared to average velocities of 1500 m/s in the literature, lower values for velocity have been determined in Fallen Leaf Lake to match reflector depths to identifiable core features (Maloney et al., 2013). Recently measured P-wave velocities from the Beaufort margin yield velocities of ~1333 m/s in fine-grained sediment (Keigwin et al., 2018). As the P-wave velocity is inversely related to density, in some shallow sedimentary environments, especially fine-grained sediments, the density increases more than the bulk modulus. As such the velocity of the shallow sediments can be lower than seawater.

4. Results

Interpretations of clinothem sequences by Slingerland et al. (2008a) were built upon and extended as the extent of their interpretations was limited to an area offshore of the Bamu and Turama rivers highlighted by white seismic track lines in Fig. 1. Here we extend these interpretations 75 km to the southwest and 50 km to the northeast to constrain the regional architecture of the clinothems in light of the different source rivers (e.g., Fig. 1). Units are defined by bounding unconformities and surfaces of lap defined by Harris et al. (1996) and Slingerland et al. (2008a) and summarized in Section 2.2. We briefly describe new observations in each unit before focusing on internal architecture and surfaces of lap within the Holocene units, architecture of the Southern, Central, and Northern lobes, facies descriptions, and Holocene chronology.

4.1. Basal sequence: Unit D (pink)

Gas wipeout obscures the internal reflectors of Unit D in many places, namely the Central and Northern lobes of the GoP clinothem. In the Southern lobe, high-amplitude reflectors that abruptly terminate due to gas wipeout are observed in Unit D (Fig. 3). Despite the dominant dip of reflectors to the east, the dips are variable along-margin. Unit D is highly deformed in the northeastern-most section of the GoP with increased deformation proximal to the thrust front (Fig. 4). A prominent antiform-synform pair in Unit D is imaged in the profile with faulting occurring mostly along the fold axis.

4.2. Unit C (blue)

Where Unit D is observed, it is mantled by Unit C. Most of Unit C is characterized by aggradational beds; however, in some regions, an increase in dip in the upper portions of the unit is observed (Fig. 3). Dipping beds are not observed regionally in the upper section of Unit C because of marked differential erosion. Where this dipping package is imaged, progradation in the along-margin direction is steeper (~2.5°) than in the across-margin direction (~0.1°). Note the marked increase in rugosity of the seafloor in regions where Unit C is exposed (Figs. 2 and 3).

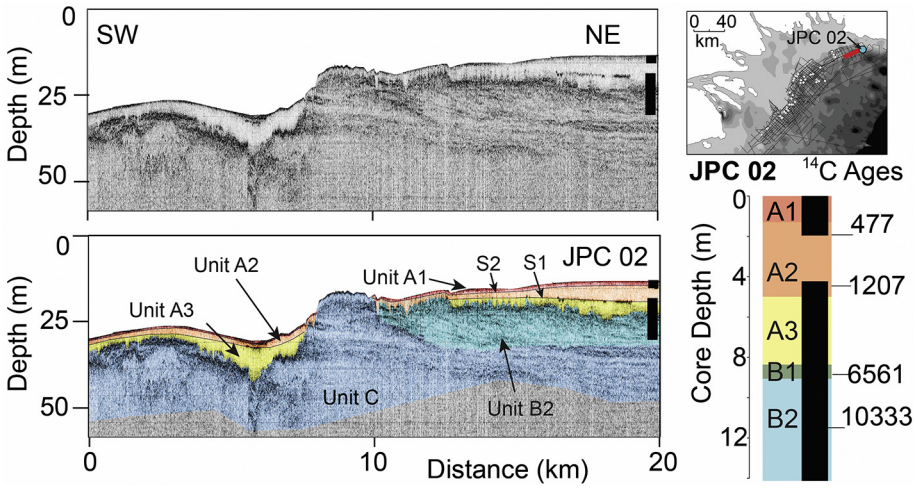

Fig. 5. Unit B2 (cyan) progrades off a topographic high to the NE. The top of the package is characterized by an undulating surface. JPC02 and trigger core recovered sediment from this deposit and is projected on the seismic profile. On the right, an expanded view JPC02 and trigger core are shown relating corrected radiocarbon ages to depositional units observed in the seismic profile. Inset shows location of seismic profile (highlighted in red) and JPC 02 (blue circle). (For interpretation of the references to color in this figure legend, the reader is referred to the web version of this article.)

4.3. Unit B2 (cyan)

Unit B2 is observed only in the northeast GoP and it exhibits subtle oblique prograding reflectors to the northeast that downlap onto Unit C (Shown as Cyan in Fig. 5). The reflectors in this deposit are tightly spaced and have lower acoustic amplitudes than the reflectors in Unit C. The upper boundary of this prograding deposit is undulatory and is ~19 m below sea level, whereas the bottom boundary of the deposit is erosional and located at ~34 m below sea level.

4.4. Unit B1 (green)

Unit B1 infills the erosional relief on the upper surface of Unit C (Fig. 2) and its thickness is predominantly controlled by the highs and lows in Unit C. In the valleys and channels, these deposits are the thickest. In the intervening highs, the deposits thin and pinch out by onlap. As described in Section 4.7, the thickness of many of the infilling deposits is close to 1 m, which approaches the imaging capability of the CHIRP system to resolve acoustic horizons. In seismic profiles, the reflectors of this deposit exhibit a variety of acoustic character. In Fig. 2, Unit B1 is acoustically transparent whereas in Fig. 4, basal reflectors in Unit B1 mimic underlying topography and upper reflectors are wavy and discontinuous. The top of this deposit is roughly horizontal; however, in localized areas, such as the northeast GoP, this deposit is deformed (Fig. 4).

4.5. Holocene clinothem: surfaces S1 and S2, Units A1, A2, and A3

Units A1, A2, and A3 are defined by the S1 and S2 bounding surfaces. The S1 and S2 surfaces of lap are by reflectors in the underlying unit exhibiting toplap against the surface of lap. Toplap is not observed in all profiles, as in the case of the dip profile in Fig. 2. Where toplap is observed, Unit A3 originates at the upper boundary of Unit C or B1 and terminates where reflectors are truncated or offlap at S1. The base of Unit A2 reflectors contact S1 by onlap or downlap and are terminated at the top of the unit by S2. Unit A1 is defined by parallel reflectors that mimic S2 with the upper boundary of Unit A1 being the seafloor.

In dip profiles where toplap is observed, toplap against S1 and/or S2 can be observed on both the clinoform topset and foreset. In Fig. 4, prograding Unit A3 reflectors exhibit toplap against the S1 surface and to the southwest, Unit A2 a prograding reflector is truncated by the S2 surface. In the southern survey area, Unit A3 exhibits toplap against S1 on the clinothem foreset (Fig. 6; Line 03, Zoom 1). In strike profiles, toplap is commonly observed on the transition from topographic high to topographic low (Fig. 6). Near the 7.4 km marker of Line 01 is a topographic high in Unit C above which the overlying Holocene units thin (Fig. 6). On the flanks of this topographic high, Unit A2 thickens and reflectors within A2 prograde to the southwest and northeast (Fig. 6). These prograding reflectors exhibit toplap against S2, as shown in Fig. 8, zooms 2 and 3. Additional examples of NE-SW prograding reflectors that exhibit toplap are shown in Fig. 6, zooms 4 and 5, where Units A3 and A2 prograde and thicken into the topographic low. The upper boundary of these prograding reflectors are terminated by the S1 and S2 surfaces, respectively (Fig. 6).

Shingling and toplap are more pronounced on clinothem topsets, as demonstrated in Line 06 from the Central Lobe (Fig. 7). In Zoom 1, a mounded feature in Unit A3 is truncated by the S1 surface. Above the mounded feature, reflectors in Unit A2 pinch out and shingle into the topographic low (Fig. 7). In Zoom 2, hummocky reflectors within Unit A3 are suggestive of a slump and bulge downward into a topographic low (Fig. 7). Where this feature mounds, the high-amplitude reflectors in Unit A3 appear to terminate up dip at the S1 surface (Fig. 7). Above the mound of Unit A3 sediment, reflectors in Unit A2 pinch out and exhibit shingling (Fig. 7). Similar patterns of toplap are observed in the topset line of the Northern lobe, where reflectors within Unit A2 are truncated by the S2 surface (Fig. 8). Unit A2 displays great variability in thickness in the Northern lobe and is likely controlled by highs and lows formed in the underlying Unit A3 deposits (Fig. 8). In the Northern lobe, hummocky reflectors within Unit A3 that build into topographic lows are observed and are interpreted as potential slumps (Fig. 8).

4.6. Holocene clinothem lobe architecture

The Holocene clinothem has three lobes, the Southern, Central, and Northern lobes that are defined by stratal geometry (Fig. 9), Holocene sediment thickness (Fig. 10A and B), and the bathymetric highs and incised valleys in Unit C (Fig. 10C). The northern edge of the Southern lobe is a promontory referred to as “the Nose” (Fig. 1) and located offshore of the northern tributary of the Fly River delta. The Central and Northern lobes are separated by a broad topographic low that is infilled with Holocene deposits thick enough to obscure the underlying Units C and D. Within the Northern and Southern lobes are valleys incised into Unit C that have not been completely infilled by Holocene sediments, creating lows in the modern day bathymetry with intervening bathymetric highs. There are two bathymetric highs (BH) in the Southern lobe and two in the Northern lobe. In contrast, valleys incised into Unit C in the Central lobe have been infilled almost completely by thick Holocene sediments.

In the Southern lobe, the southernmost bathymetric high (Line 01, SH1) shoals to a minimum depth of −23.6 m. Moving north, the adjacent BH (Line 02, SH2) shoals to ~12 m, which is the shallowest bathymetric high along the entire margin and creates a shallow

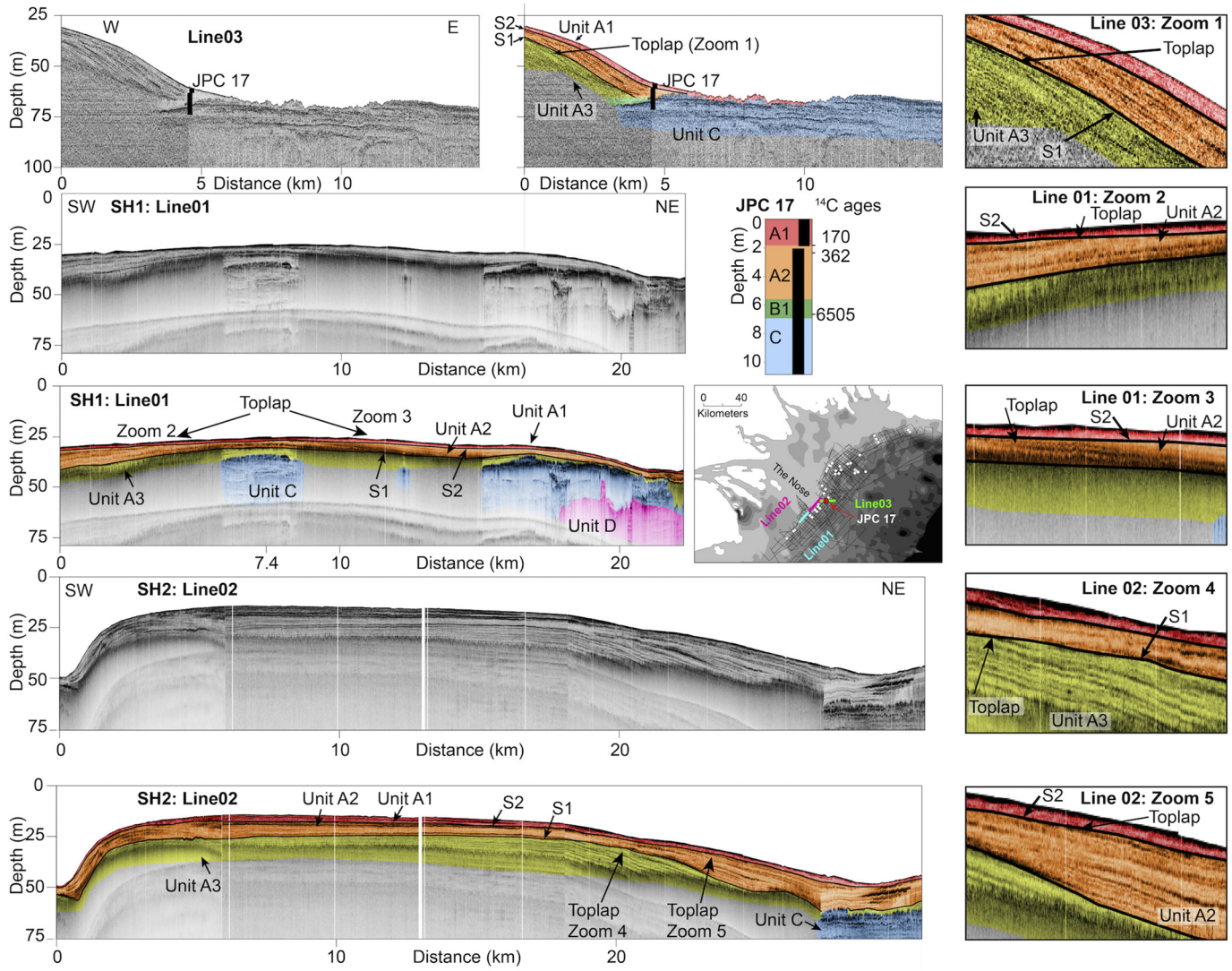

Fig. 6. Seismic profiles in the Southern Lobe exhibit toplap. Top: line 03 shows toplap in Unit A3. Bottomsets of A3, A2, and A1 are sampled by JPC 17. Corrected radiocarbon dates are shown on units identified in the seismic profiles. Middle: Holocene clinothem is thinner across sublobe SH1. Toplap is observed in Unit A2 on line 1. Bottom: Holocene clinothem is thicker to the north in SH2 with pronounced toplap in Units A3 and A2. Inset map locates seismic profiles. At right are enlargements of areas that exhibit toplap against the S1 and S2 surfaces.

promontory (i.e., the Nose; Figs. 1 and 6). Holocene sediment cover is thin on the SH1 promontory. Conversely, across the SH2 promontory, Unit A3 thickens. Unit A2 does not thicken on topographic highs but instead exhibits oblique progradation into the adjacent topographic lows, such as along the southwest flank of SH1 and the northeast flank of SH2. Unit A2 displays along-margin thickness variability and toplap at the highs of both bathymetric highs beneath the S2 boundary (Fig. 6 middle and bottom, Fig. 9B).

Due to infilling of incised valleys in Unit C by thick Holocene sediment cover, the Central lobe has only one bathymetric high (Figs. 7 and 9C). Infilling of valleys by Unit A3 is predominantly aggradational in strike lines (Fig. 7). Northeast of the Central lobe, A3 and A2 thicken and prograde into the low separating the Central and Northern lobes (Fig. 7). On topographic highs, there is no observed toplap in Unit A2 against the S2 boundary. Two regions of deformed sediment within Unit A3 are observed in the southwest and northeast portions of the Central lobe. An antiform-shaped feature with discontinuous, wavy reflectors is observed in the southwest (Fig. 9C). The upper reflectors in the antiform are truncated by the S1 surface. On top of this surface of lap lies a thin veneer of aggrading Unit A2.

The Northern lobe is composed of two bathymetric highs: NH1 in the southwest and NH2 in the northeast (Figs. 8 and 9D). No toplap is observed in Unit A3. The reflectors within Unit A2 aggrade on NH1 and prograde into the low between NH1 and NH2 (Fig. 8). Where Unit A2 progrades into the low, it exhibits toplap, as the Blue and Lime green internal reflectors are truncated by the S2 surface (km 20 in Fig. 10). Thick deposits and gas wipeout limit the imaging of the Unit C in the Northern lobe.

4.7. Holocene clinothem dip variability along the margin

The slopes of the upper boundaries of Units A3, A2, and A1 exhibit along-margin variability throughout the clinothem foresets (Table 2; Fig. 11). Note that the upper boundary of Unit A1 is the seafloor, the upper boundary of A2 is S2, and the upper boundary of A3 is S1. Foreset slopes are the steepest at the seafloor and systematically diminish downsection to the upper surface of Unit A3. Slopes from Table 2 reveal that slopes are steepest within the Southern and Northern lobes, with the lowest slopes located within the Central lobe. Given the lobate geometry of the GoP clinothem, we measured slopes on profiles that were located near the center of the bathymetric high and within a bathymetric low. The Southern lobe exhibits the largest difference in

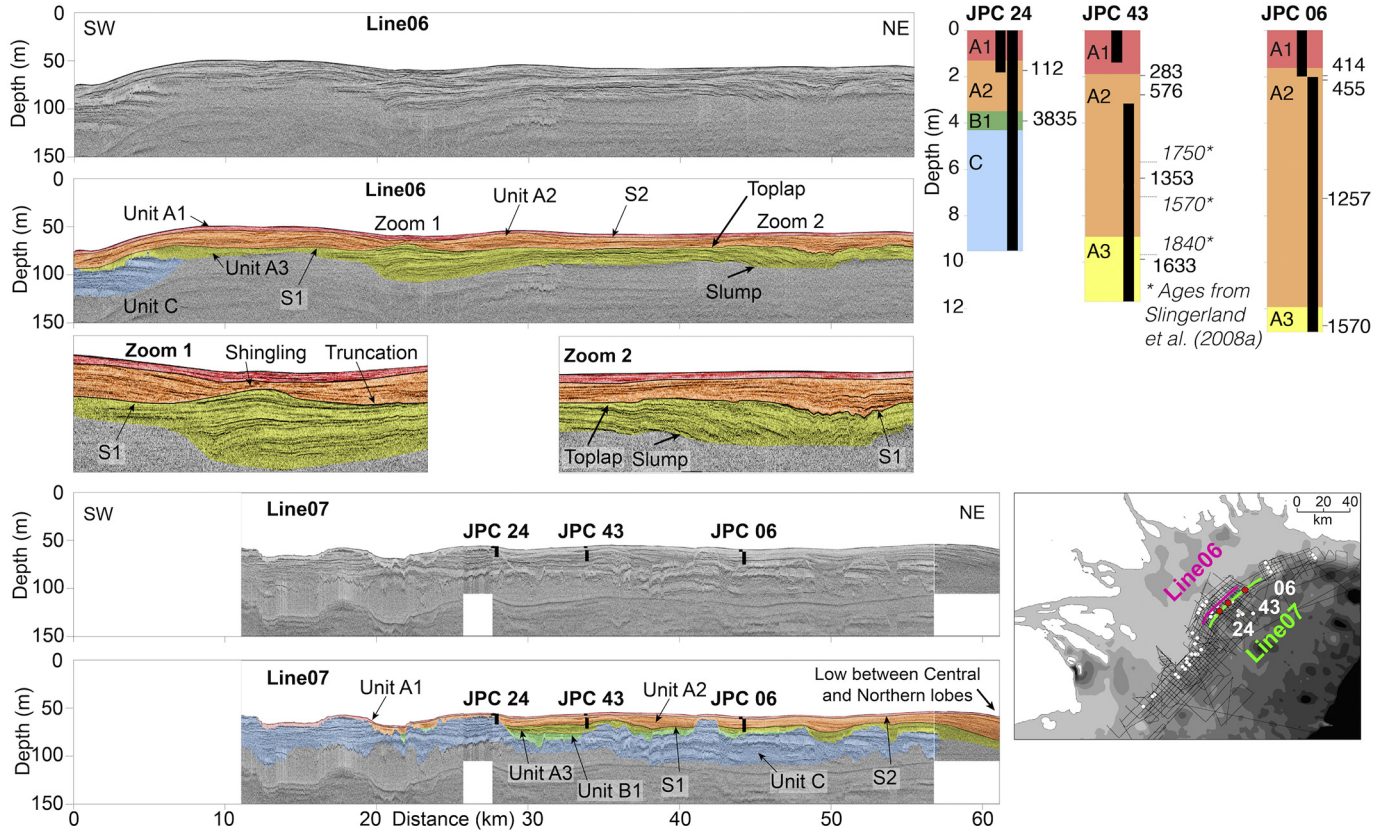

Fig. 7. Strike profiles from the Central Lobe. Top: line 06 across the foreset illustrates aggradational Units A3 and A2. Reflectors in Unit A2 exhibit no toplap. Below the seismic profile, two zooms enlarge areas that exhibit shingling, truncation, toplap, or slumping. The area of enlargement is labeled on the seismic profile. Bottom: Line 07 acquired across the bottomset images valleys incised into Unit C with aggrading infill. JPCs 24, 43, and 06 are located on this line. Corrected radiocarbon dates are shown on units identified in the seismic profiles. JPC 43 also shows radiocarbon ages from Slingerland et al. (2008a). Below, map locates the two seismic profiles and three cores.

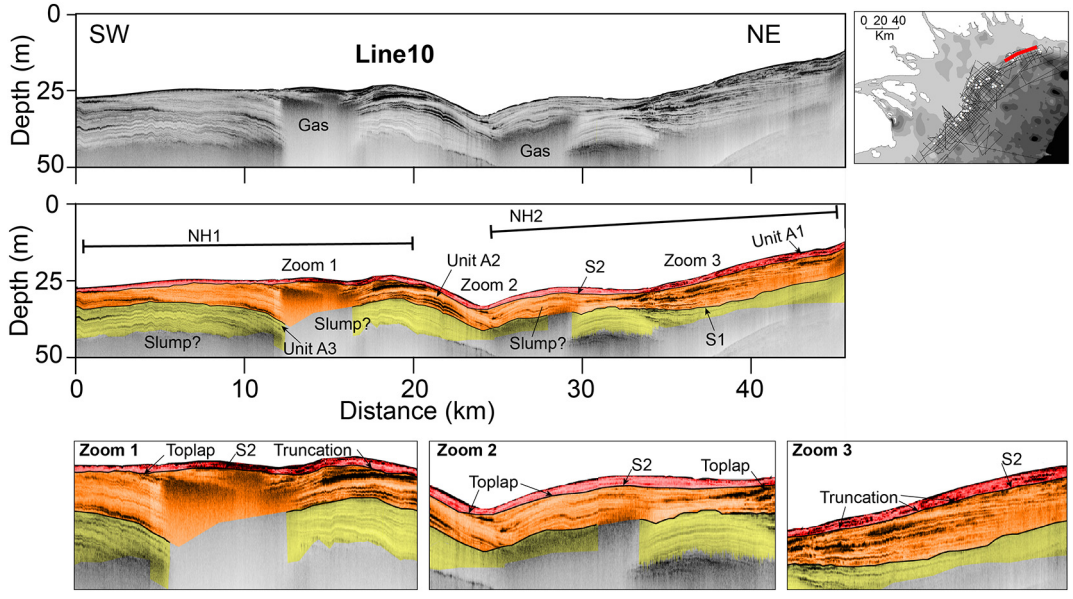

Fig. 8. Strike line 10 located on the upper foreset of the Northern lobe. Unit A3 and A2 exhibit internal deformation characteristic of a slump deposit. Note thick deposits and gas wipeout obscure underlying Unit C. Inset at right: red line shows the location of strike profile. Below, three enlargements of areas that exhibit toplap. The area of enlargement is labeled on the seismic profile. (For interpretation of the references to color in this figure legend, the reader is referred to the web version of this article.)

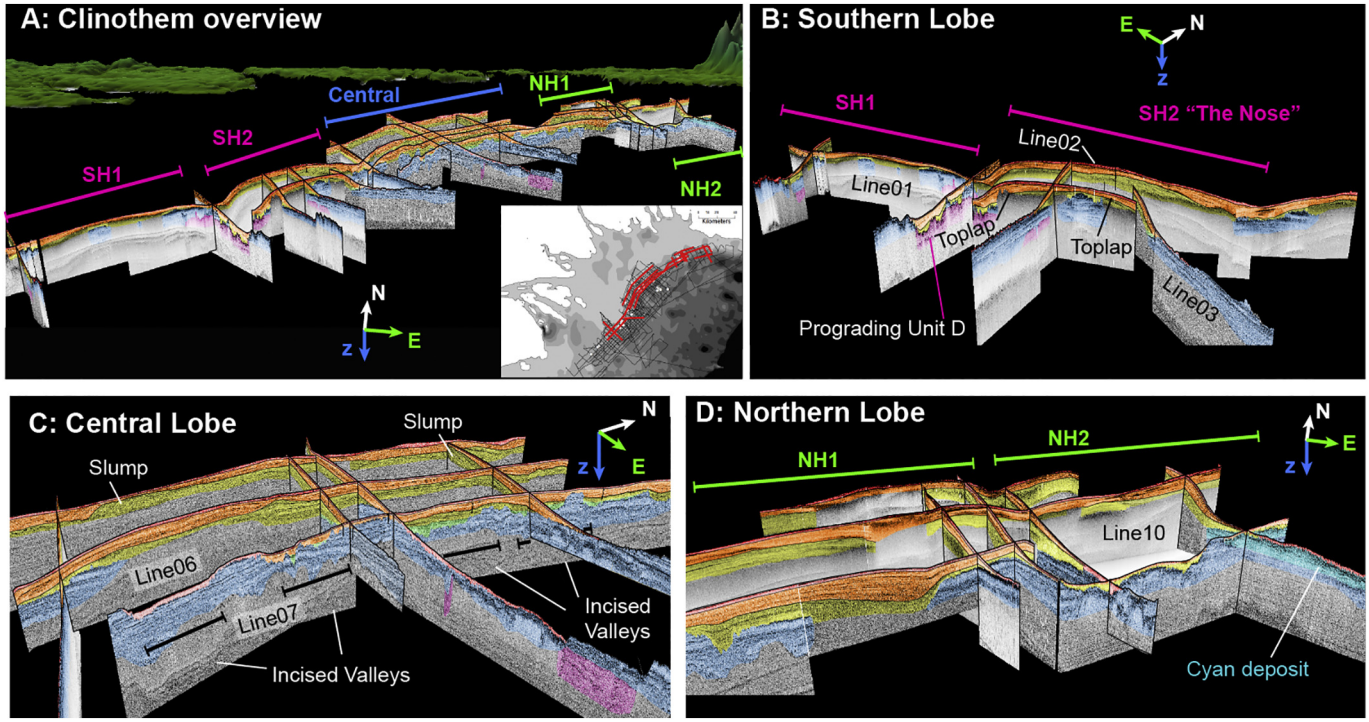

Fig. 9. A) Fence diagram of the GoP clinothem shows the three main lobes and their sublobes. Inset: red lines show location of fence diagram. B) Fence diagram of the Southern Lobe and its bathymetric highs SH1 and 2. Lines 01, 02, and 03 are shown in Fig. 6. C) Fence diagram of the Central Lobe shows incised valleys are filled by aggradational deposits. Two deformed regions are observed in the southwest and northeast and are interpreted to be slump deposits. Lines 06 and 07 are shown in Fig. 7. D) Fence diagram of the Northern Lobe and its two bathymetric highs NH1 and 2. Unit B2 (cyan) is located on the northeast edge of NH2. Line 10 is shown in Fig. 8. (For interpretation of the references to color in this figure legend, the reader is referred to the web version of this article.)

slope between bathymetric highs and lows (0.154° for the seafloor), whereas the Northern and Central lobes have lower differences between bathymetric highs and lows (0.025° and 0.005° for respective seafloor slopes). Our range of seafloor slopes are comparable to those measured in the high-energy Amazon subaqueous clinothem that reported a range of slopes between 0.06 and 1.15° with an average of 0.29° (Nittrouer and DeMaster, 1996). Steeper seafloor slopes were reported in the shallow-water Atchafalaya subaqueous delta of 0.10–0.11° (Neill and Allison, 2005). Seafloor foreset slopes in the GoP are lower than the global average of foreset slopes of muddy delta-scale subaqueous deltas at ~0.76° but are within the global range of 0.03–6° (Patruno et al., 2015).

4.8. Core facies

Unit D was recovered only in JPC 36, where the sediment facies is homogenous mud interbedded with sand lenses that are ~0.5–1 cm thick (Fig. 12A). Cores recovered from Unit C consist of a mud matrix with interbedded sand lenses and this unit was recovered at the bottom of JPCs 17, 21 and 24. In JPC 21, this sequence consists of 0.5–1 cm thick sand lenses separated by layers of mud 20–30 cm thick (Fig. 12B). In JPC24, Unit C is dominated by a mud matrix with centimeter-thick sand lenses separated by tens of centimeters of mud (Fig. 12C). In this core, the sand lenses are medium-grained sand.

Unit B2 sediment is markedly different from those in Unit C and was recovered only at the base of JPC02. This deposit has dominantly dark sands and mud lenses at intervals of 1–2 cm. The matrix sand is dark colored (7.5R3/0) and has higher magnetic susceptibility (MS) values of 60 to 200 $_{E}{}^{-8}$ SI (m^3/kg) in comparison to Unit C MS values in the range of 20 to 80 $_{E}{}^{-8}$ SI (m^3/kg).

Unit B1 was recovered in cores JPC02, JPC17, JPC21, and JPC24. In all of these cores, this deposit is represented by mud with coarse-grained sands containing shell fragments (Fig. 12E, F). In cores, the thickness of Unit B1 ranges from 0.70 m in the Northern lobe, 0.3–0.62 m in the Central lobe, and 0.26–1.13 m in the Southern lobe. Based on the cores, Unit B exhibits little variation in sediment thickness along the margin across topographic highs or within lows; however, more cores recovered B1 deposits in the Southern lobe than in the Central and Northern lobes. The boundary between Unit B1 and A3 is transitional from more abundant sand and shell lag deposits in B1 to less abundant sand and shell material in Unit A3. This transition can be up to a few decimeters thick.

Holocene units A1, A2, and A3 are distinct in seismic profiles; however, they do not appear to correlate with any observed grain size differences in the cores. Instead, facies and grain size variability within the Holocene units appear more dependent on core location, whether it be on the topset, foreset, or bottomset. Topset facies are characterized by more abundant sand lenses, whereas foreset and bottomset facies have few sand stringers. The topset cores GC31 and GC23 are composed of a mud matrix with abundant 0.5–1 cm thick sand lenses (Fig. 12G, H). In contrast, foreset cores JPC02 and JPC22 contain mostly silty mud with sparse sand lenses (Fig. 12J, K). The bounding surfaces of lap S1 and S2 do not correlate with detectable changes in grain size or facies.

4.9. Chronostratigraphy and sedimentation rates of Units B2, B1 and Holocene sequences

Benthic foraminifera were sampled from Units B2, B1, A3, A2, and A1 and were radiocarbon dated. Corrected and uncorrected ages, depth in core, and sediment unit are described in Table 3. Only one sample from Unit B2 was recovered, yielding an age of 10.33 ka (Table 3; Fig. 5). Ages of Unit B1 range from the youngest at 3835 years BP to the oldest at 6561 years BP (Table 3; Figs. 2, 5, 6, and 7).

The Holocene sequence has ages spanning from modern sediment at the sediment surface to the oldest collected age of 1633 years BP. No ages were recovered in the uppermost Unit A1. An age of 170 years BP

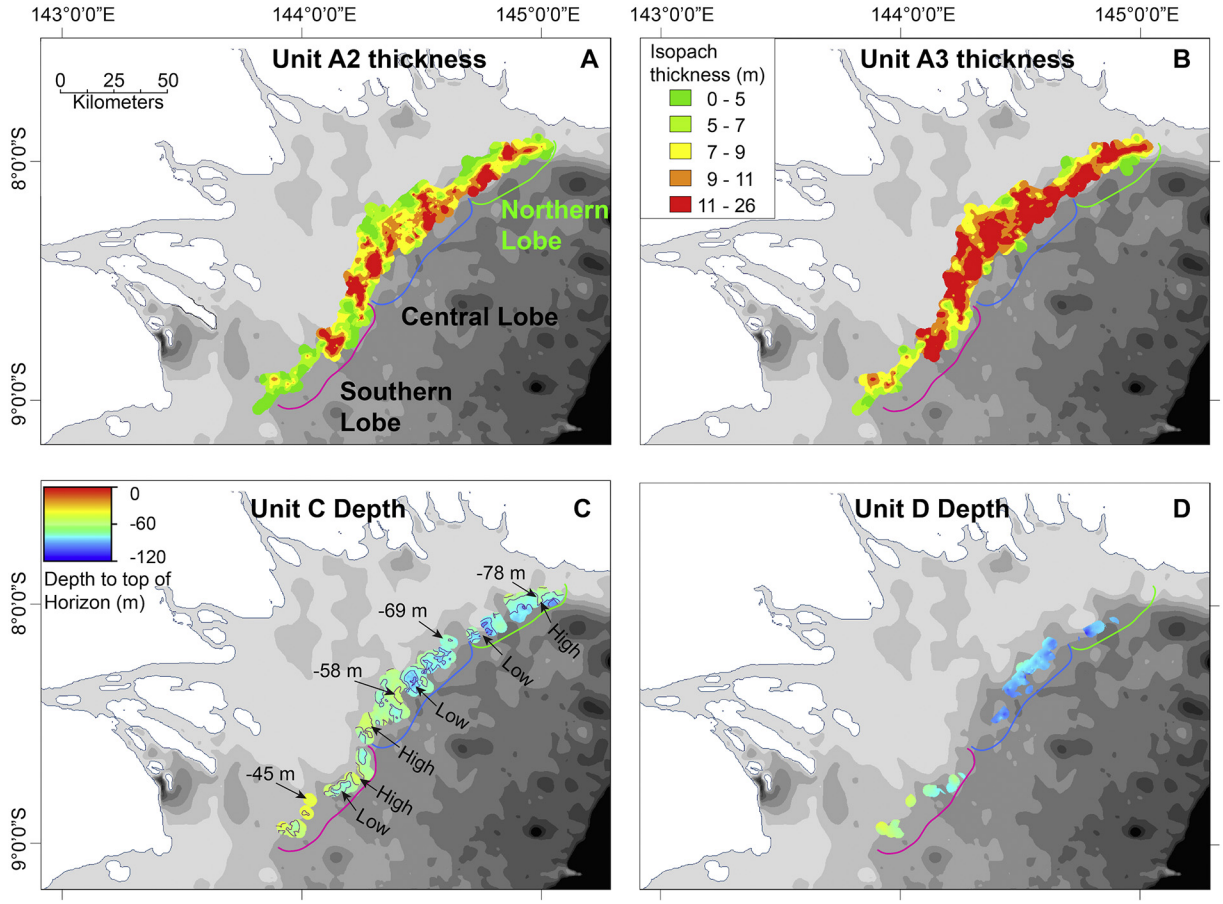

Fig. 10. Isopach maps of sediment thickness; map A shows Unit A2 (orange) and Map B shows yellow Unit A3 packages. Note the thickness of Unit A3 is greater than A2 and is more uniformly distributed, whereas the thickness in Unit A2 is more localized because sediment is prograding off the topographic highs. On the bottom are structure contour maps of the surfaces of the (C) Unit C and (D) Unit D sequences. The depth to Units C and D systematically increase to the northeast. (For interpretation of the references to color in this figure legend, the reader is referred to the web version of this article.)

Table 2
The slopes of the upper surfaces of Units A1, A2, and A3.

Line	Seafloor (A1) foreset (°)	A2 foreset (°)	A3 foreset (°)	Lobe	Bathymetric High/Low
Line04	0.446	0.421	0.370	Southern	High
Line05	0.292	0.257	0.153	Southern	Low
Line08	0.182	0.144	0.121	Central	High
Line09	0.187	0.198	0.173	Central	Low
Line12	0.262	0.250	0.184	Northern	High
Line11	0.287	0.260	0.219	Northern	Low

is located just below the A1 and A2 boundary (S2) in JPC 17 (Table 3; Fig. 6). In JPC 24, the youngest date in Unit A2 is dated at 112 years BP (Table 3, Fig. 7). The boundary between Units A2 and A3, or the S1 surface, is dated between 1353 and 1570 years BP.

Sedimentation rates were calculated for units that had two or more ages and no rates were calculated across package boundaries. Sedimentation rates for Unit A2 in bottomset cores (all except for JPC 22) range from 2.83–6.36 mm/yr. Downcore sedimentation rates in A2 from JPCs 06 and 43 are higher than those upsection (Table 3). Radiocarbon dates from JPC 22 reveal that sedimentation rates for Unit A2 are an order of magnitude higher than other rates for the same package; however, it is the only dated core located on the clinothem foreset. The only sedimentation rate calculated for Unit B1 is in JPC 21 and is an order of magnitude lower than rates determined for Unit A2.

5. Discussion

We present a conceptual model for the timing of Units B2, B1, A3, A2, and A1. In light of the revised chronostratigraphic framework for deposits in the GoP, we will focus on parameters that control the architecture of the Holocene clinothem, such as tectonic deformation, sediment supply, and oceanographic forcing.

5.1. Updated chronostratigraphy

By using radiocarbon dates and a balance between sediment supply and eustatic sea level changes, we develop a relative stratigraphy for Unit C. We also agree with the relative depositional timing of Unit D proposed by Slingerland et al. (2008a). We also agree with the depositional timing proposed by Harris et al. (1996) and Slingerland et al. (2008a) for Unit C; however, their age estimates are significantly older than published ages from Howell et al. (2014) from Unit C. Previous radiocarbon age determinations for Unit C exhibit quite a wide range in ages, with Harris et al. (1996) dating an intact bivalve (articulated) to yield an age of 26,900 years BP and Howell et al. (2014) dating mollusk fragments and ooids to yield inverted ages in the core ranging from 8400 to 9350 years BP (Fig. 2). The ages from Howell et al. (2014) may not be reliable because the vital effects of molluscs are poorly known and ooids have concentric growth rings. In light of these considerations, we prefer the interpretations from Harris et al. (1996) and Slingerland et al. (2008a) that Unit C was formed during MIS 3.

For the Holocene units, core sampling and radiocarbon dates provide a more quantitative age model. Unit B2 mantles Unit C and is

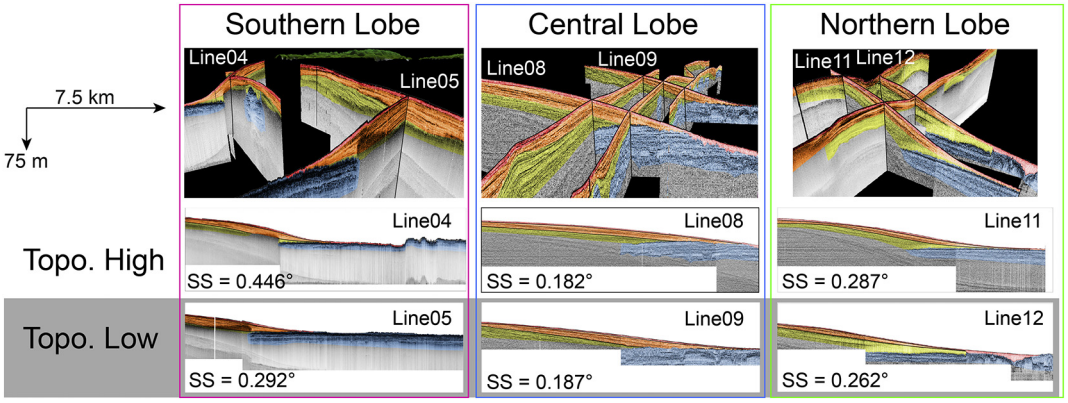

Fig. 11. Selected dip lines from the topographic highs and lows for the Southern, Central, and Northern lobes. In the Southern and Northern lobes, the dip profiles across the topographic highs have steeper seafloor slopes (SS) than the profiles across the topograhic lows. In contrast, the Central lobe exhibits little change in dip across the topographic high and low. The steepest seafloor slopes are observed in the Southern lobe and the most gentle slopes observed in the Central lobe. Scale shown is for all dip profiles.

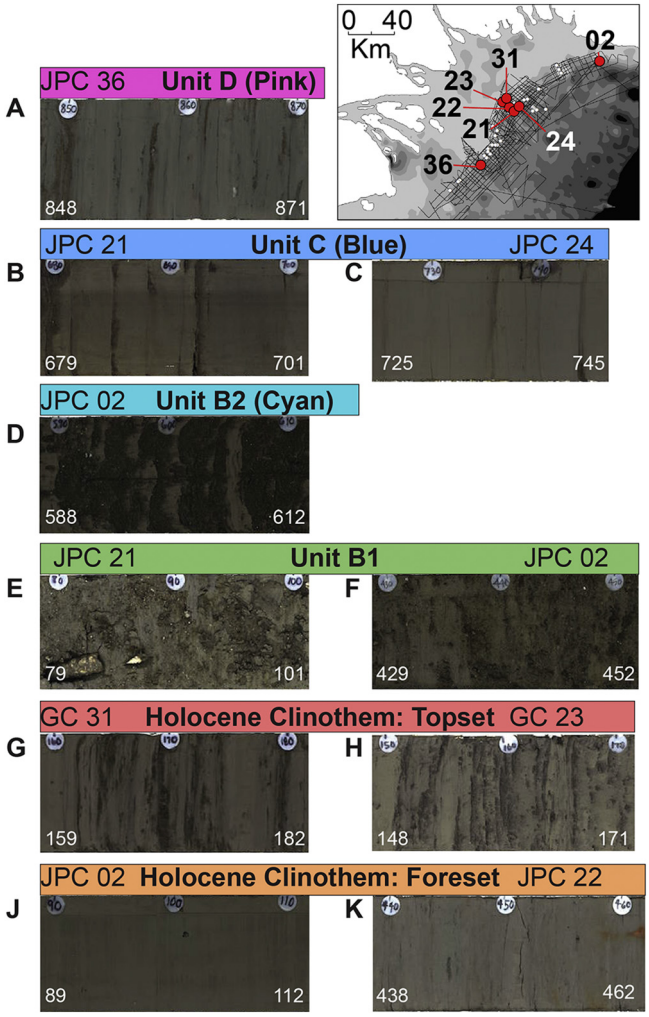

Fig. 12. Photos of facies observed in cores. Plastic circles mark 10-centimeter intervals in the core. Photo intervals are annotated at the bottom corners of each photo. Sand stringers interspersed with mud layers are observed in Unit D, Unit C, and the Holocene clinothem topset (A, B, C, G and H). The Holocene clinothem foreset is characterized by only occasional sand stringers (J, K). The transgressive gravel and shell lag of Unit B1 separates Unit C from the Holocene clinothem (E, F). Next to A, the inset map shows the locations of the cores.

beneath the maximum flooding surface. Thus, we postulate that Unit B2 was deposited during the sea level transgression after MIS 2. Radiocarbon ages from Table 3 and an age of 9500 years BP from Slingerland et al. (2008a) lead us to propose that Unit B2 was deposited during Holocene sea level rise around 10.3–9.5 ka (Fig. 13).

The chronostratigraphy of Unit B1 was first discussed by Harris et al. (1996), who acquired uncorrected radiocarbon ages from this deposit ranging from 16,750–7290 years BP. These ages are much older than the uncorrected radiocarbon ages reported here, and the older ages could reflect redeposition of older peat deposits. Radiocarbon dating constrains the timing of deposition for Unit B1 to be between 3835 and 6561 years BP. Slingerland et al. (2008a) reported a 5.21 ka age measured on a bivalve sample recovered from the overlying Holocene Unit A3. Given the age is older than determined for the underlying Unit B, we propose that the bivalve may be sourced from reworked material older than the age of deposition. The ages reported here are from benthic foraminifera, which are more likely to be closer to the depositional age. Based on the younger radiocarbon ages, we propose that Unit B1 is younger than 6.5 ka and that the overlying Holocene sequence is younger than 3.8 ka (Fig. 13).

We propose a younger depositional age for the Holocene sequence, as our ages are younger than those acquired by Slingerland et al. (2008a) on bulk carbonate samples for JPC 43 consisting of shelf fragments, ooids, and other material (Fig. 9). In all likelihood, they represent reworked debris, which would explain the older ages than the benthic foraminifera ages reported in this study. Our refined chronostratigraphy dates the S1 surface (Units A3–A2) between 1353 and 1570 years BP. This surface of lap was not likely caused by sea level, given there are no meltwater pulses or stillstands during this time period.

5.2. Transgressive deposits

The shell lag and coarse sand within Unit B1 was likely eroded from tidal deposits from an inner estuary, as suggested by Harris et al. (1996). The mixture of this material within a matrix of silts and clays suggests that Unit B1 is a lag deposit derived from wavebase erosion and reworking of upslope material. As Unit B1 was deposited between 3.8 and 6.5 ka when sea level rose following MIS 2, this unit is interpreted as a transgressive lag. Overlying Unit B1 is the transgressive surface that separates subaerially exposed sediments below from marine sediments above. In seismic profiles, horizontal reflectors in Unit B1 are observed below the transgressive surface and above it Unit A3 reflectors exhibit downlap. In sediment cores, the transgressive surface appears as a gradual grain size and shell abundance transition as described in Section 4.8.

Table 3
Radiocarbon ages shown with their sequence or package. Sedimentation rates were calculated within packages. Ages denoted with a single asterisk (*) were published by Slingerland et al. (2008a). Listed ages with two asterisks (**) were published by Howell et al. (2014).

Core	Depth (mbsf)	Corrected ^{14}C age	Uncorrected ^{14}C age	Error ± (year BP)	Unit	Sedimentation rate (mm/yr)
JPC 02	1.85	477	860	43	A2	3.58
	4.46	1207	1655	38	A2	
	8.86	6561	6140	54	B1	
	13.66	10,333	9480	100	B2	
JPC 06	1.95	414	785	21	A2	3.90
	2.11	455	830	27	A2	6.36
	7.21	1257	1710	46	A2	
	12.71	1570	2015	40	A3	
JPC 17	1.83	170	550	30	A1/A2	2.71
	2.35	362	725	16	A2	
	6.65	6505	6090	46	B1	
JPC 21	1.64	204	585	35	A2	3.44
	1.85	265	630	37	A2	
	2.27	4259	4185	30	B1	0.18
	2.50	5518	5165	30	B1	
	2.9	9350**	8820		C	
	3.5	8400**	8070		C	
	4.4	8806**	8250		C	
JPC 22	1.80	334	690	30	A2	20.69
	4.20	450	825	35	A2	
JPC 24	1.73	112	500	13	A2	
	3.87	3835	3880	46	B1	
JPC 43	1.95	283	645	38	A2	2.83
	2.78	576	995	27	A2	4.63
	5.68	1750*			A2	
	6.38	1353	1820	30	A2	
	7.18	1570*			A2	
	9.68	1840*			A3	
	9.88	1633	2070	35	A3	

Given Unit B2's localized deposition in the northeast GoP, we postulate that Unit B2 could be tidal channel fill in an inner estuary environment. Tidal channels can have high sedimentation rates, are composed of medium-grained cross-bedded sand with mud, and have cross-bedded laminae due to undulatory tidal flow (Allen and Posamentier, 1994). Similar sequences of estuarine facies onlapping onto tidal channel facies have been documented in boreholes and seismic profiles in the Sabine River Valley (Thomas and Anderson, 1994), the Gironde River Estuary (Allen and Posamentier, 1994), the Guadiana Estuary (Lobo et al., 2003), and the Eel margin (Hogarth et al., 2012). We hypothesize that the undulatory upper boundary of Unit B2 likely represents sediment waves, which could be formed by bidirectional tidal flow. Differences in depositional environments cause resulting disparities in lithologies and thicknesses between the two transgressive deposits. Unit B2 infilled existing physiography whereas B1 is formed by transport of reworked material seaward.

5.3. Holocene clinothem architecture

Growth of the older Holocene A3 unit was likely controlled by changes in thickness of the underlying Unit C and thus water depth. Our observations that Unit C exerts controls on the overlying Holocene clinothem is consistent with the concept of a foundation surface (or "depositional foundation") that stresses the importance of the surface morphology onto which a clinoform is emplaced (Helland-Hansen and Gjelberg, 1994; Helland-Hansen and Martinsen, 1996; Cattaneo et al., 2007). The foundation surface concept introduces two factors relevant in the GoP that may influence younger deposition: 1) the importance of

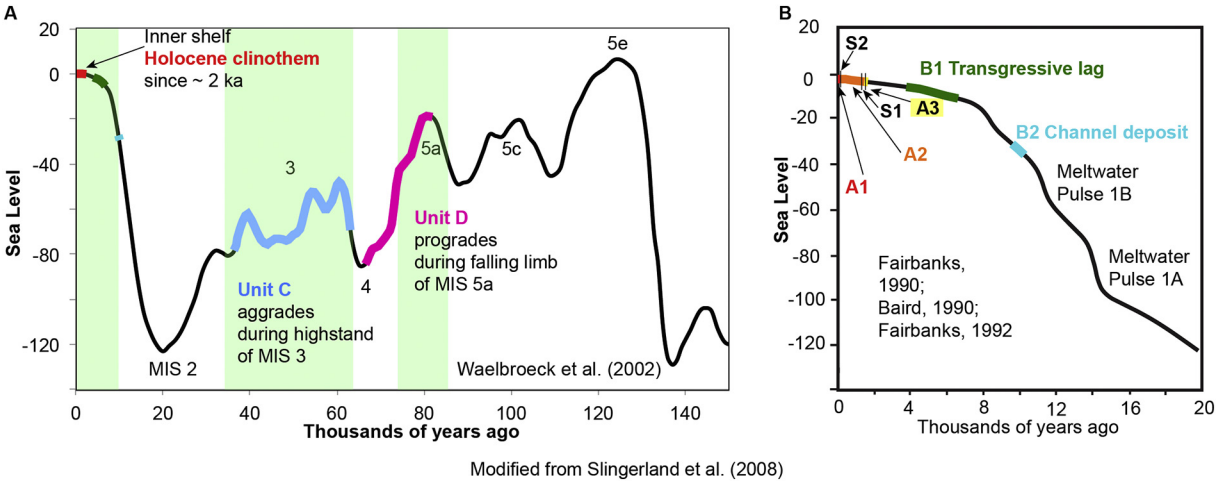

Fig. 13. Two sea level curves are shown for the last 150 kyr (A) and the last 20 kyr (B). Depositional timing based off sequence stratigraphic principles is shown for the Units C and D. Based off new radiocarbon ages, the depositional timing is shown for Units B2, B1, A3, A2, A1, S2, and S1.

the depth of the surface onto which the progradational wedge advances and 2) that preexisting depressions may be preferentially filled compared to adjacent zones (Cattaneo et al., 2007). Units A3 and A2 are very much influenced by the depth of the foundation surface, as more shingling and toplap occurs in the Southern lobe with a shallower foundation surface and more aggradation occurs in the Northern lobe with a deeper foundation surface. The isopach map of Unit A3 (Fig. 10B) reveals that thick A3 deposits exist in both topographic lows and highs and are connected across the corrugated topography (Fig. 10B). As Unit A3 is first deposited, it preferentially infills preexisting depressions into Unit C, and thus is consistent with the foundation surface concept (Helland-Hansen and Gjelberg, 1994; Helland-Hansen and Martinsen, 1996; Cattaneo et al., 2007). Preferential infilling into local depressions is also observed on the Adriatic margin (Cattaneo et al., 2007). Once these incised valleys were preferentially filled, fluid-mud processes may have acted on these recent Unit A3 deposits and allowed for across-margin progradation of A3 sediment across the foreset. The across-margin orientation of these conduits could have caused Unit A3 to prograde preferably across- rather than along-margin. After Unit A3 infilled these across-margin valleys, across-margin fluid-mud transport for Unit A2 may not have been as effective. As a result, Unit A2 does not prograde seaward much farther than A3.

Unit A2 thickens into the topographic lows creating bullseye patterns of discontinuous thick deposits in topographic lows (Fig. 10A). Note differences in the isopach maps between continuous Unit A3 deposits and patchy A2 deposits. Minimal seaward progradation of A2 could result from oceanographic processes that prograde A2 obliquely northeast, as described in Section 5.3.1.

5.3.1. Oceanographic controls on along-margin geometries

Along-margin profiles of the Holocene clinothem throughout the entire GoP reveal oblique growth in the northeast-southwest direction as observed in Unit A2 (Figs. 6, 7, and 8). Our stratigraphic observations agree with hydrographic interpretations from Walsh et al. (2004) and Slingerland et al. (2008b). Aggradation and temporary deposition of sediment on topographic highs likely occurs during the Monsoon season, which has lower energy bottom currents. Strengthening of near-bed currents during the Trade wind season winnows and reworks sediment on the topographic highs. Northeast bottom currents active during the Trade wind season advect sediment, causing it to prograde into topographic lows. The net sediment transport shifts the topographic highs to the northeast, as a result building the clinothem obliquely (Fig. 10A). Oblique progradation of A2 off the preexisting highs into the corrugated morphology controls the bulls-eye patterns observed in the isopachs by thinning deposits on the topographic highs. Thus, the current seasonal circulation patterns in the Gulf of Papua have likely persisted since inception of Unit A2.

Convergence of flow localizes sedimentation in SH2 (Slingerland et al., 2008b) and may be responsible for creating a depocenter at SH2 or “the Nose”. Flow convergence may cause further feedbacks where sediment deposition causes features to grow and shoal, thus altering local circulation and allowing for the persistence of gyres (Figs. 6 and 10A).

5.3.2. Foreland basin subsidence, accommodation, and surfaces of lap

Subsidence of the northern GoP and peripheral bulge uplift of the southern GoP have influenced Holocene clinothem growth since they engender more accommodation in the north and less in the south. These tectonic processes may modulate the depth of the foundation surface, which in turn can exert influences on depositional regimes of the overlying Holocene clinothem, as shallower foundation surfaces are exposed to higher shear stresses than deeper foundation surfaces (Cattaneo et al., 2007). Deformation of GoP sediment by foreland basin subsidence is evidenced in Fig. 4, where faults cross-cut reflectors in Unit D (Fig. 4). Another line of evidence for foreland basin subsidence is that depth to the upper surface of Units D and C are deeper in the Northern lobe than in the Southern and Central lobes (Fig 10C and D). Unit C is observed at depths of −45 m in the Southern lobe and at depths of −78 m in the Northern lobe (Fig. 10C). Unit C beds are horizontal to sub-horizontal throughout the margin, suggesting that subsidence occurred after deposition. The observed deepening of Units C and D may record footwall loading associated with GoP foreland basin subsidence in the northern GoP, whereas the southwest GoP is located closer to the peripheral bulge and is thus undergoing less subsidence (Fig. 1; Pigram et al., 1989). As tectonic deformation and differential subsidence are orthogonal to the eustatic plane, the eustatic and tectonic signals can be deconvolved. The difference in depth between the Southern and Northern lobes suggests that since the LGM, the topography has undergone differential subsidence of ~33 m, yielding an average subsidence rate of 1.65 mm/a. This is comparable to the rate calculated from Slingerland et al. (2008a). In contrast, subsidence rates during the Pliocene calculated from stratigraphic thicknesses from DSDP Site 209 are an order of magnitude larger (Davies et al., 1989). Additional research and deeper imaging seismic reflection data are required to understand the decrease in subsidence rates since the Pliocene.

Differential subsidence of the foreland basin creates more accommodation in the northeast than in the southwest and as a result it influences reflector geometry in the Holocene clinothem. In the Southern lobe, with the least amount of accommodation, Units A3 and A2 exhibit toplap in SH1 and SH2 (Fig. 6). SH2 is shallower than SH1, and thus SH2 is exposed to higher bottom stresses and exhibits more toplap. In contrast, the Central and Northern lobes have deeper Unit C, with the reflectors in the Holocene clinothem characterized predominantly by aggrading reflectors in their sublobes (Figs. 7 and 8). In the Central lobe, toplap is observed only in Unit A3 truncating the upper reflectors of slumped deposits (Figs. 7 and 10C). Farther north, toplap is only exhibited in the topset of NH1 within Unit A2 of the Northern lobe (Fig. 8).

Seismic strike profiles through the topset exhibit more toplap than those in the foreset or bottomset. Toplap is evidence of a nondepositional hiatus (likely due to bypass) caused by a lack of accommodation to permit aggradation (Mitchum et al., 1977a; Christie-Blick and Driscoll, 1995). It is likely that toplap is more prevalent on topsets because of reduced accommodation, increased exposure to wave energy, and larger bed shear stresses. As a result, suspended sediment concentration above the bed is higher on the topsets than on the foresets (Walsh et al., 2004). Suspended sediment above the topset beds could form fluid mud, which under high bed shear stresses could be remobilized, bypass the topset, and be deposited farther downslope. This process may cause toplapping reflectors to pinch out upsection (Christie-Blick and Driscoll, 1995). Sediment bypass at topset beds was also suggested by Walsh et al. (2004), who observed that topset cores have reduced sediment accumulation rates. Gradients in energy regimes from the topset to the bottomset affect the accumulation of sediment, downdip variations in reflector thickness, and physical sediment properties.

Surfaces of lap observed throughout the survey area are recognized mainly in seismic profiles and are not discernable in sediment cores. As truncation of underlying layers by S1 and S2 is most commonly observed on clinothem topsets, it is likely that the S1 and S2 surfaces represent erosive boundaries rather than flooding surfaces. Based off radiocarbon dates of the S1 and S2 surfaces, Slingerland et al. (2008a) proposed that S1 was caused by a decline in sediment supply. Given the S1 surface is dated between 1353 and 1570 years BP, a time of no sea level stillstands (Fig. 13), we propose that S1 in the Southern lobe is due to the local interplay between decreased paleowater depths and increased bottom stresses. In the Central lobe, thick Unit A3 slump deposits (Figs. 7 and 9C) could have filled available water depth, thus preventing further sediment accumulation and promoting bypass. Since the S2 surface separating Units A2 and A1 is younger than at least 112 years BP, this surface is not likely a result of decreased sediment

supply as was proposed by Slingerland et al. (2008a), since sediment accumulation during this period likely increased as a result of anthropogenic impacts (Haberle, 1998). Instead, the S2 surface is also likely formed by decreased paleowater depths and increased bottom stresses.

Interpreting S1 and S2 as margin-wide surfaces of lap caused by sea level and sediment supply is difficult, as the S1 and S2 surfaces are not continuous surfaces found throughout the GoP Holocene clinothem. Toplap against the S1 and S2 surfaces where observed appear to separate Holocene packages; however, such geometry is not observed throughout the Holocene clinothem. When examining the different lobes of the Holocene clinothem and toplap geometry, it appears to record a local interplay between paleowater depths and oceanographic currents.

5.3.3. Implications: relationship of along-margin and across-margin geometry

Slopes of the upper boundary of Units A3, A2, and A1 exhibit variations along the GoP (Table 2, Fig. 11). Cross-sectional clinothem dips may be controlled by a number of complex factors including grain size, clinothem height, oceanographic energy and sediment dispersal regimes, and basin physiography (Pirmez et al., 1998; Driscoll and Karner, 1999; Cattaneo et al., 2003, 2007; Swenson et al., 2005; Patruno et al., 2015). The variability in the GoP may reflect a number of factors, including the location of the profile, location within a bathymetric high or low, accommodation created by foreland basin subsidence, sediment supply, and the dispersal of sediment by oceanographic currents. In the Central lobe, across-margin clinothem profiles have the shallowest slopes, whereas the steepest across-margin slopes are observed in the Southern lobe (Table 2; Fig. 11). The Central Lobe is located at the depocenter of the margin-wide clinothem where accumulation rates are the highest (Walsh et al., 2004; Slingerland et al., 2008a,b). Thick sediment deposits in the Central lobe diminish the relief of the underlying physiography. As a result, differences in slope between the topographic highs and lows are minimal (0.005° difference in the seafloor slopes). In the Northern lobe, clinothem slopes appear to be steeper than those in the Central lobe. Steeper slopes may be a consequence of topset aggradation in the Northern lobe that is enabled by more accommodation. Model simulations from Driscoll and Karner (1999) reveal that when the rate of sediment supply is subordinate to the rate of new accommodation, clinothems aggrade faster than prograde, thus causing downslope thinning and the steepening of each successive clinothem. Such is the case with clinothems in the Northern lobe that exhibit thinning near the bottomset (Line 12, Fig. 11). As a result of deeper clinothem rollovers in the Northern lobe, Northern lobe topsets may be deeper than the wave-base and as a result may not experience the shear stresses necessary for sediment resuspension, as evidenced by aggradational topsets in Lines 11 and 12 (Fig. 11). Sediment normally supplied to the foreset via fluid-mud may be diminished in the Northern lobe. Thus, vertically aggrading topsets and diminished foreset progradation may be the cause of steeper clinothem slopes in the Northern lobe.

Large differences in slope between the topographic highs and lows in the Southern lobe reflect interplays between lower sediment supply and the convergence of currents around the Nose (SH2). Low sediment supply to this region (Walsh et al., 2004; Palinkas et al., 2006) is unable to infill uneven topography, creating large height differences between the topographic highs and lows. Sediment that is supplied to this region is redirected to SH2 instead of SH1 due to the convergence of currents. As a result, these currents build a localized depocenter at SH2 and engender large height differences between SH1, SH2, and the topographic low between them. This illustrates that in the Southern lobe, steep slopes are likely caused by uneven topography dividing the two sublobes and variable sediment distribution due to the convergence of currents toward SH2.

The balance between sediment supply, accommodation, and the influence of the underlying Unit C controls Holocene clinothem slopes. Steepness and geometry of clinothems change with along-margin transport processes, and thus down-slope clinothem geometry can be misinterpreted as changes in sediment supply or relative sea level. Thus, the traditional two-dimensional approach to interpreting clinothems as a rate-related geometry between accommodation and sediment supply needs to incorporate additional processes that alter three-dimensional clinothem geometry.

6. Summary and conclusions

Analysis of modern clinothem stratal architecture illustrates the importance of circulation, preexisting physiography, and differential subsidence in their development.

1. Chronology of several units was redefined from those of Slingerland et al. (2008a) by extensive radiocarbon dating within Units B1, B2, and the Holocene clinothem. Depositional timing of the Holocene clinothem was found to be younger than reported in previous studies because material sampled (e.g., shell fragments, bivalves, peat, wood) by Slingerland et al. (2008a) appear to have been reworked when compared to dates derived from benthic foraminifera. As the ages of surfaces of lap are not coincident with sea level stillstands or meltwater pulses, these surfaces are not likely caused by eustatic sea level changes, as was previously suggested.
2. The basal Unit D (Pink) has been subject to deformation, such as folding and faulting, associated with foreland basin tectonics. Valleys incised into Unit C affect the flow of bottom currents on the shelf and also create localized increases in paleowater depth in the intervening lows. Subsidence of Units C and D has created more accommodation in the northeast and less in the southwest. Toplap is more extensive in the shallow Southern lobe and in topset beds, which are to be subjected to higher bed shear stresses (Walsh et al., 2004) and may experience more bypass or non-deposition.
3. Thicknesses and geometries of Holocene units may be influenced by interplays between the corrugated topography and oceanographic currents. Isopach maps of Unit A3 show that depocenters are more interconnected, as there were large paleowater depths in the topographic lows. Thus A3 maintains topography with slightly more deposition in the topographic lows. Elevated topographic highs constructed by A3 increase bottom shear stresses such that Unit A2 progrades to the northeast, infilling the adjacent topographic lows. Unit A2 preferentially infills the topographic lows and is winnowed off the topographic highs, creating a bullseye appearance in the isopach map.
4. Though the S1 and S2 surfaces of lap are identified by toplap, toplap is not universally present throughout the Holocene clinothem. As such, toplap probably is not caused by margin-wide processes such as sea level stillstands or decreased sediment supply but is rather influenced by local interplays between paleowater depths and oceanographic currents.
5. Downdip clinothem slopes are shallowest in the Central Lobe and show the greatest difference between topographic highs and lows in the Southern Lobe. The traditional rate-related problem of interpreting clinothem geometry is further complicated in settings with current-controlled sediment advection. In these locations, along-margin controls on sediment dispersal need to be considered.

Controls exerted by tectonic deformation, bottom currents, and inherited physiography can be isolated in the GoP because the deformation and currents are normal to eustatic sea level changes. However, this configuration is not observed at many margins. As mentioned above, there are many instances of clinothems extending downdrift in response to along-margin currents, such as in Rio de Janeiro (Reis et al., 2013), the Adriatic Sea (Cattaneo et al., 2003), and offshore of the Yangtze River (Xu et al., 2009). Additionally, some margins exhibit along-margin tectonic deformation, such as the case of offshore La

Jolla, California (Hogarth et al., 2007; Le Dantec et al., 2010) and the Eel Margin in northern California (Hogarth et al., 2012). Clinothem growth should be analyzed in three-dimensions on continental margins and could be further aided by three-dimensional modeling studies (e.g., Driscoll and Karner, 1999).

Acknowledgements

This research was funded by the National Science Foundation awards 0305699, 0305779, and 0305607 under the MARGINS Source to Sink program. Special thanks to the crew of the R/V Melville as their efforts allow scientists access to the sea. Craig Fulthorpe, Claudio Pellegrini, Hector Perea, and two anonymous reviewers provided salient and helpful reviews that improved the quality of the manuscript. Rachel Marcuson and Ana Martini aided in sampling benthic foraminifera for radiocarbon dating. GMT was used to construct isopach and structural contour maps.

References

Allen, G.P., Posamentier, H.W., 1994. Transgressive Facies and Sequence Architecture in Mixed Tide-and Wave-dominated Incised Valleys: Example From the Gironde Estuary, France.

Cattaneo, A., Carreggiari, A., Langone, L., Trincardi, F., 2003. The late-Holocene Gargano subaqueous delta, Adriatic shelf: sediment pathways and supply fluctuations. Mar. Geol. 193, 31.

Cattaneo, A., Trincardi, F., Asioli, A., Correggiari, A., 2007. The Western Adriatic shelf clinoform: energy-limited bottomset. Cont. Shelf Res. 27, 506–525.

Christie-Blick, N., Driscoll, N.W., 1995. Sequence stratigraphy. Annu. Rev. Earth Planet. Sci. 23, 451–478.

Cohen, J., Stockwell Jr., J., 2001. CWP/SU: Seismic Unix Release 35: A Free Package for Seismic Research and Processing. Center for Wave Phenomena, Colorado School of Mines.

Davies, H.L., 2012. The geology of New Guinea-the cordilleran margin of the Australian continent. Episodes 35, 87–102.

Davies, P.J., Symonds, P.A., Feary, D.A., Pigram, C.J., 1989. The evolution of the carbonate platforms of northeast Australia. 44, 26.

Day, G., Dietrich, W.E., Rowland, J.C., Marshall, A., 2008. The depositional web on the floodplain of the Fly River, Papua New Guinea. J. Geophys. Res. 113.

Dietrich, W., Day, G., Parker, G., 1999. The Fly River, Papua New Guinea: inferences about river dynamics, floodplain sedimentation and fate of sediment. In: Varieties of Fluvial Form, pp. 345–376.

Driscoll, N.W., Karner, G.D., 1999. Three-dimensional quantitative modeling of clinoform development. Mar. Geol. 154, 15.

Haberle, S.G., 1998. Late Quaternary vegetation change in the Tari Basin, Papua New Guinea. Palaeogeogr. Palaeoclimatol. Palaeoecol. 137, 1–24.

Harris, P.T., Baker, E.K., Cole, A.R., Short, S.A., 1993. A preliminary study of sedimentation in the tidally dominated Fly River Delta, Gulf of Papua. Cont. Shelf Res. 13, 32.

Harris, P., Pattiaratchi, C., Keene, J., Dalrymple, R., Gardner, J., Baker, E., Cole, A., Mitchell, D., Gibbs, P., Schroeder, W., 1996. Late Quaternary deltaic and carbonate sedimentation in the Gulf of Papua foreland basin: response to sea-level change. J. Sediment. Res. 66.

Harris, P.T., Hughes, M.G., Baker, E.K., Dalrymple, R.W., Keene, J.B., 2004. Sediment transport in distributary channels and its export to the pro-deltaic environment in a tidally dominated delta: Fly River, Papua New Guinea. Cont. Shelf Res. 24, 2431–2454.

Helland-Hansen, W., Gjelberg, J.G., 1994. Conceptual basis and variability in sequence stratigraphy: a different perspective. Sediment. Geol. 92, 31–52.

Helland-Hansen, W., Martinsen, O.J., 1996. Shoreline trajectories and sequences; description of variable depositional-dip scenarios. J. Sediment. Res. 66, 670–688.

Henkart, P., 2003. SIOSEIS Software. Scripps Inst. of Oceanogr, La Jolla, Calif available at. http://sioseis.ucsd.edu.

Hogarth, L.J., Babcock, J., Driscoll, N.W., Le Dantec, N., Haas, J.K., Inman, D.L., Masters, P.M., 2007. Long-term tectonic control on Holocene shelf sedimentation offshore La Jolla, California. Geology 35, 275–278.

Hogarth, L.J., Driscoll, N.W., Babcock, J.M., Orange, D.L., 2012. Transgressive deposits along the actively deforming Eel River Margin, Northern California. Mar. Geol. 303, 99–114.

Howell, A.L., Bentley, S.J., Xu, K., Ferrell, R.E., Muhammad, Z., Septama, E., 2014. Fine sediment mineralogy as a tracer of latest Quaternary sediment delivery to a dynamic continental margin: Pandora Trough, Gulf of Papua, Papua New Guinea. Mar. Geol. 357, 108–122.

Keen, T.R., Ko, D.S., Slingerland, R.L., Riedlinger, S., Flynn, P., 2006. Potential transport pathways of terrigenous material in the Gulf of Papua. Geophys. Res. Lett. 33.

Keigwin, L.D., Klotsko, S., Zhao, N., Reilly, B., Giosan, L., Driscoll, N.W., 2018. Deglacial floods in the Beaufort Sea preceded Younger Dryas cooling. Nat. Geosci. 11, 599–604.

Kineke, G., Sternberg, R., Trowbridge, J., Geyer, W., 1996. Fluid-mud processes on the Amazon continental shelf. Cont. Shelf Res. 16, 667–696.

Kuehl, S.A., Nittrouer, C.A., Demaster, D.J., 1986. Distribution of sedimentary structures in the Amazon subaqueous delta. Cont. Shelf Res. 6, 311–336.

Kuehl, S.A., Levy, B.M., Moore, W.S., Allison, M.A., 1997. Subaqueous delta of the Ganges-Brahmaputra river system. Mar. Geol. 144, 81–96.

Le Dantec, N., Hogarth, L.J., Driscoll, N.W., Babcock, J.M., Barnhardt, W.A., Schwab, W.C., 2010. Tectonic controls on nearshore sediment accumulation and submarine canyon morphology offshore La Jolla, Southern California. Mar. Geol. 268, 115–128.

Liu, J., Xue, Z., Ross, K., Wang, H., Yang, Z., Li, A., Gao, S., 2009. Fate of sediments delivered to the sea by Asian large rivers: long-distance transport and formation of remote alongshore clinothems. Sediment. Rec. 7, 4–9.

Lobo, F., Dias, J., González, R., Hernández-Molina, F., Morales, J., Del Río, V.D., 2003. High-resolution seismic stratigraphy of a narrow, bedrock-controlled estuary: the Guadiana estuarine system, SW Iberia. J. Sediment. Res. 73, 973–986.

Maloney, J.M., Noble, P.J., Driscoll, N.W., Kent, G.M., Smith, S.B., Schmauder, G.C., Babcock, J.M., Baskin, R.L., Karlin, R., Kell, A.M., 2013. Paleoseismic history of the Fallen Leaf segment of the West Tahoe–Dollar Point fault reconstructed from slide deposits in the Lake Tahoe Basin, California-Nevada. Geosphere 9, 1065–1090.

Marcuson, R.K., Gee, J.S., Driscoll, N.W., 2018. An AMS Study of Gulf of Papua Ocean Sediment Cores-Evidence of Deformation Caused by Piston Coring, presented at 2014 Fall Meeting, AGU, San Francisco, California, 15-19 December, Abstract GP23B-3687.

Martin, D.P., Nittrouer, C.A., Ogston, A.S., Crockett, J.S., 2008. Tidal and seasonal dynamics of a muddy inner shelf environment, Gulf of Papua. J. Geophys. Res. 113 (F1).

McHugh, C.M., Hartin, C.A., Mountain, G.S., Gould, H.M., 2010. The role of glacio-eustasy in sequence formation: Mid-Atlantic Continental Margin, USA. Mar. Geol. 277, 31–47.

Milliman, J.D., 1995. Sediment discharge to the ocean from small mountainous rivers: the New Guinea example. Geo-Mar. Lett. 15, 127–133.

Mitchum Jr., R., Vail, P., Thompson III, S., 1977a. Seismic stratigraphy and global changes of sea level: part 2. The depositional sequence as a basic unit for stratigraphic analysis: section 2. In: Application of Seismic Reflection Configuration to Stratigraphic Interpretation.

Mitchum Jr., R., Vail, P., Sangree, J., 1977b. Seismic stratigraphy and global changes of sea level: part 6. Stratigraphic interpretation of seismic reflection patterns in depositional sequences: section 2. In: Application of Seismic Reflection Configuration to Stratigraphic Interpretation.

Neill, C.F., Allison, M.A., 2005. Subaqueous deltaic formation on the Atchafalaya Shelf, Louisiana. Mar. Geol. 214, 411–430.

Nguyen, V.L., Ta, T.K.O., Tateishi, M., 2000. Late Holocene depositional environments and coastal evolution of the Mekong River Delta, Southern Vietnam. J. Asian Earth Sci. 18, 427–439.

Nittrouer, C.A., DeMaster, D.J., 1996. The Amazon shelf setting: tropical, energetic, and influenced by a large river. Cont. Shelf Res. 16, 21.

Nittrouer, C.A., Wright, L.D., 1994. Transport of particles across continental shelves. Rev. Geophys. 32, 85–113.

Nittrouer, C., Curtin, T., DeMaster, D., 1986. Concentration and flux of suspended sediment on the Amazon continental shelf. Cont. Shelf Res. 6, 151–174.

Ogston, A.S., Sternberg, R.W., Nittrouer, C.A., Martin, D.P., Goñi, M.A., Crockett, J.S., 2008. Sediment delivery from the Fly River tidally dominated delta to the nearshore marine environment and the impact of El Niño. J. Geophys. Res. 113.

Palinkas, C., Nittrouer, C., Walsh, J., 2006. Inner-shelf sedimentation in the Gulf of Papua, New Guinea: a mud-rich shallow shelf setting. J. Coast. Res. 760–772.

Patruno, S., Helland-Hansen, W., 2018. Clinoform systems: Review and dynamic classification scheme for shorelines, subaqueous deltas, shelf edges and continental margins. Earth Sci. Rev. 185, 202–223.

Patruno, S., Hampson, G.J., Jackson, C.A., 2015. Quantitative characterisation of deltaic and subaqueous clinoforms. Earth Sci. Rev. 142, 79–119.

Pigram, C., Symonds, P., 1991. A review of the timing of the major tectonic events in the New Guinea Orogen. J. SE Asian Earth Sci. 6, 307–318.

Pigram, C.J., Davies, P.J., Feary, D.A., Symonds, P.A., 1989. Tectonic controls on carbonate platform evolution in southern Papua New Guinea: passive margin to foreland basin. Geology 17, 199–202.

Pirmez, C., Pratson, L.F., Steckler, M.S., 1998. Clinoform development by advection-diffusion of suspended sediment: modeling and comparison to natural systems. J. Geophys. Res. Solid Earth 103, 24141–24157.

Puig, P., Ogston, A.S., Guillén, J., Fain, A.M.V., Palanques, A., 2009. Sediment transport processes from the topset to the foreset of a crenulated clinoform (Adriatic Sea). Cont. Shelf Res. 27 (3-4), 452–474.

Reimer, P.J., Bard, E., Bayliss, A., Beck, J.W., Blackwell, P.G., Bronk Ramsey, C., Buck, C.E., Cheng, H., Edwards, R.L., Friedrich, M., 2013. IntCal13 and Marine13 Radiocarbon Age Calibration Curves 0–50,000 Years Cal BP.

Reis, A.T., Maia, R.M.C., Silva, C.G., Rabineau, M., Guerra, J.V., Gorini, C., Ayres, A., Arantes-Oliveira, R., Benabdellouahed, M., Simões, I., Tardin, R., 2013. Origin of step-like and lobate seafloor features along the continental shelf off Rio de Janeiro State, Santos basin-Brazil. Geomorphology 203, 25–45.

Ritchie, B.D., Gawthorpe, R.L., Hardy, S., 2004. Three-dimensional numberical modeling of deltaic depositional sequences 1: influence of the rate and magnitude of sea-level change. J. Sediment. Res. 74, 17.

Slingerland, R., Driscoll, N.W., Milliman, J.D., Miller, S.R., Johnstone, E.A., 2008a. Anatomy and growth of a Holocene clinothem in the Gulf of Papua. J. Geophys. Res. 113.

Slingerland, R., Selover, R.W., Ogston, A.S., Keen, T.R., Driscoll, N.W., Milliman, J.D., 2008b. Building the Holocene clinothem in the Gulf of Papua: an ocean circulation study. J. Geophys. Res. 113.

Stuiver, M., Polach, H.A., 1977. Discussion reporting of 14 C data. Radiocarbon 19, 355–363.

Swenson, J.B., Paola, C., Pratson, L., Voller, V.R., Murray, A.B., 2005. Fluvial and marine controls on combined subaerial and subaqueous delta progradation: morphodynamic

modeling of compound-clinoform development. J. Geophys. Res. Earth Surf. 110.
Tcherepanov, E.N., Droxler, A.W., Lapointe, P., Dickens, G.R., Bentley, S.J., Beaufort, L., Peterson, L.C., Daniell, J., Opdyke, B.N., 2008. Neogene evolution of the mixed carbonate-siliciclastic system in the Gulf of Papua, Papua New Guinea. J. Geophys. Res. 113.
Thomas, M.A., Anderson, J.B., 1994. Sea-level Controls on the Facies Architecture of the Trinity/Sabine Incised-valley System, Texas Continental Shelf.
Vail, P.R., Mitchum Jr., R., Thompson III, S., 1977. Seismic stratigraphy and global changes of sea level: part 3. Relative changes of sea level from Coastal Onlap: section 2. In: Application of seismic reflection Configuration to Stratigraphic Interpretation.
Walsh, J.P., Nittrouer, C.A., Palinkas, C.M., Ogston, A.S., Sternberg, R.W., Brunskill, G.J., 2004. Clinoform mechanics in the Gulf of Papua, New Guinea. Cont. Shelf Res. 24, 2487–2510.
Warrick, J.A., Mertes, L.A.K., Washburn, L., Siegel, D.A., 2004. Dispersal forcing of southern California river plumes, based on field and remote sensing observations. Geo-Mar. Lett. 24, 46–52.
Wolanski, E., Alongi, D., 1995. A hypothesis for the formation of a mud bank in the Gulf of Papua. Geo-Mar. Lett. 15, 166–171.
Wolanski, E., Norro, A., King, B., 1995. Water circulation in the Gulf of Papua. Cont. Shelf Res. 15, 185–212.
Xu, K., Milliman, J.D., Li, A., Paul Liu, J., Kao, S.-J., Wan, S., 2009. Yangtze- and Taiwan-derived sediments on the inner shelf of East China Sea. Cont. Shelf Res. 29, 2240–2256.